Submitted to J. Climate on 9 June 2014

A further Study of ENSO Rectification: Results from an OGCM with a Seasonal cycle

Lijuan Hua[1,2], Yongqiang Yu[1], De-Zheng Sun[3]

1. State Key Laboratory of Numerical Modeling for Atmospheric Sciences and Geophysical Fluid Dynamics (LASG), Institute of Atmospheric Physics, Chinese Academy of Sciences, Beijing 100029, China
2. College of Earth Science, University of Chinese Academy of Sciences, Beijing 100049, China
3. CIRES, University of Colorado and NOAA/ESRL, Boulder, Colorado, USA

ABSTRACT

The potential role that rectification of ENSO plays as a viable mechanism to generate climate anomalies on the decadal and longer time-scales demands a thorough study of this process. In this paper, rectification of ENSO was further studied using an Ocean GCM that has a realistic seasonal cycle. In addition to conducting a pair of forced ocean GCM experiments with and without ENSO fluctuations as done in a previous study, we have also conducted a forced experiment with the sign of wind anomalies reversed, with the goal to clarify the role of the asymmetry in the wind forcing and more generally to better understand the nonlinear dynamics responsible for the rectification. We find that the rectification effect of ENSO is to cool western Pacific warm-pool, warm the equatorial eastern Pacific.

We further find that when the sign of the wind stress anomalies is reversed, the impact of the rectification on the mean state remains almost unchanged. This lack of change is further explained by noting that the upper ocean temperature and velocity anomalies (t',u',v',w') are found to respond to the wind stress anomalies linearly except for the strongest El Nino years. Thus the correlation between t' and (u',v',w') (and thus the nonlinear dynamical heating) remains the same when the sign of the wind stress anomalies is reversed. Indeed, the spatial patterns of nonlinear dynamical heating (NDH) in all four seasons is found to resemble the rectified effect of ENSO in the mean temperature field in the respective seasons, indicating the critical rule (NDH)

in the rectification.

Key words: ENSO rectification, nonlinear dynamics, respond linearly, seasonal cycle

1. Introduction

Since Bjerknes (1969) linked El Nino to the large-scale air-sea interaction in the tropical Pacific, the El Nino-Southern Oscillation (ENSO) has been extensively studied. Many aspects of ENSO dynamics have been understood. For example, the rapid growth of an ENSO SST anomaly is linked to a positive feedback loop among SST, the surface winds, and ocean dynamics (Bjerknes 1969) .The transition between an El Nino event and a La Nina event has been explained as a linear oscillator that involves the upper ocean dynamics—the Delayed Oscillator (Suarez and Schopf 1988; Battisti and Hirst 1989) which emphasizes the reflection of the equatorial waves—and the Recharge-Discharge Oscillator (Jin 1997) which underscores more the importance of the subsurface heat content. Attempting to understand the birth of ENSO in the framework of a dynamical system, Sun (1997) links ENSO to a nonlinear response of the coupled system to the intensity of the tropical heating, raising a potential role of ENSO events in the long-term heat balance of the tropical Pacific.

The role of the ENSO events in the long-term heat balance of the tropical Pacific and more generally the question regarding the time-mean effect of ENSO was picked up in the study of Sun et al. (2004) and Sun and Zhang (2006). They conducted numerical experiments to illustrate that the response in the upper ocean temperature to an increase in the tropical radiative heating is much different between the case with ENSO and without ENSO. They suggested that the time-mean effect of ENSO is to cool the western Pacific warm-pool, warm the subsurface thermocline water as well as

the most surface tropical eastern ocean. Using a more sophisticated model, Yu and Sun (2009) also found that in response to perturbations in the extratropical region, the changes in the time-mean structure of the equatorial upper ocean are very different between the case in which ocean-atmosphere is coupled over the equatorial region and the case decoupled.

To delineate the time-mean effect of ENSO events more clearly, Liang et al. (2012) employ another approach: they quantify the time-mean effect of ENSO by contrasting the equilibrium state of the coupled tropical ocean-atmosphere with the actual realized climatology. At the equilibrium of the system, ENSO as an instability has not manifested while in the actual realized climatology ENSO has manifested. Thus, the difference between the two is a good measure of the ENSO effect in the climatology. Indeed, they have succeeded in doing such analysis with the use of an analytical model. The model is a highly simplified representation of the coupled tropical ocean-atmosphere system, but it encapsulates the major physics of the ENSO system. In the context of this model, they show unambiguously that the time-mean effect of ENSO is a warming to the eastern tropical Pacific (Fig. 2), supporting the earlier results of Sun (2003) and Sun and Zhang (2006) as well as the earlier inference made from the ENSO asymmetry (Jin et al. 2003, Rodger et al. 2004, Schopf and Burgman 2006). Liang et al. (2012) has also noted a correspondence between the degree of asymmetry of ENSO and its time-mean effect in the nonlinear box model for the tropical Pacific, but they show that this correspondence occurs not because the former causes the latter,

but because they are both caused by the nonlinear term in the heat budget equation. Note that although the asymmetry of ENSO was first suggested as a mechanism for the time-mean effect of ENSO events, the asymmetry alone is not a sufficient condition for a significant time-mean (or rectification) effect of ENSO because such a residual effect will depend quantitatively on how one defines El Nino and La Nina events.

The simplicity of the model used by Liang et al. (2012), however, does not give the corresponding meridional structure of the warming, limiting the full application of the mechanism revealed in that model to the observed decadal warming. Sun et al. (2014) (hereafter referred to as SZ2014) then employed another methodology to delineate the effect of ENSO events on the time-mean state of the equatorial upper ocean. This new methodology is to contrast the time-mean state of two forced ocean GCM experiments. In one experiment, the long-term mean surface wind stress is used while in the other the surface wind stress has interannual fluctuations. The two runs have identical long-term mean surface wind stress. The two runs are also restored to the same prescribed SST. So the thermal boundary conditions are such that they will damp any differences between the model and prescribed SSTs resulting from the differences in the variance in the surface winds through upper ocean dynamics in these two experiments. By having more realistic ENSO events in the simulation and the use of a GCM to provide the spatial structure of the time-mean effect of ENSO events, this new methodology compliments the earlier strategies used in examining the response

of the mean climate to a perturbation to the heat budget of the tropical Pacific using a coupled model (Sun 2003, Sun and Zhang 2006) and the method of differencing the time-mean state from the equilibrium state of the tropical Pacific using an analytical model (Liang et al. 2012).

The paper would follow the methodology used in SZ2014, but using a more sophisticated ocean model. We want to find out whether SZ2014's results dependent on the specific ocean model used. Also, the present model has a realistic seasonal cycle, which allows to address specifically whether the results of SZ2014 will be seasonally dependent. In addition, SZ2014 does not quantify the relative contribution of the asymmetry of wind stress and nonlinear ocean dynamics to the rectification. To demonstrate the critical role of upper ocean dynamics, we design another new experiment to aid understanding, in which the interannual monthly anomalies are reversed so that the contribution of the asymmetry of wind stress to ENSO dynamics can be isolated. Consequently, the mechanism of the rectification will be delineated in more great detail. The paper is organized as follows. Section 2 exhibits the methodology. Section 3 presents the main results. Conclusion is provided in section 4.

In addition to the line of research we have just reviewed above and will follow in the present study, there are also more empirically based studies of the time-mean effect of ENSO. For example, Rodger et al. (2004) find in a long simulation by a coupled GCM that changes in the mean state between decades with high ENSO activity and

decades with low ENSO activity resemble the residual of the two phases of ENSO in the model. They thereby suggest that the asymmetry could be a mechanism for decadal changes in the tropical Pacific SST. Noting a 15 year cycle in the level of ENSO activity in an extended SST data set consisting of historical and paleo-climate data, and a change in the asymmetry of ENSO with this decadal cycle, Sun and Yu (2009) has argued that the residual effect from the ENSO asymmetry may provide an explanation for the decadal cycle they have noted in the level of ENSO activity. Yu and Kim (2011) have further investigated the decadal variability in CMIP3 models from the angle of ENSO asymmetry. These studies are empirical, and as we have remarked that the asymmetry of ENSO by itself does not necessarily imply a significant time-mean effect. More recently, an analysis of the tropical Pacific decadal variability in a 2000-year integration with the Geophysical Fluid Dynamics Laboratory Climate (Delworth et al. 2006, Wittenberg 2009) Model had been conducted by Ogata et al. (2013). They found ENSO amplitude modulation is highly correlated with the second EOF mode of tropical Pacific decadal variability, which suggests that the rectified effect of ENSO is significant.

Understanding the time-mean effect of ENSO is important to understand decadal climate changes in the tropical Pacific including the decadal modulation of ENSO variance (Liang et al. 2012, Ogata et al. 2013, SZ2014). As the global warming is experiencing a hiatus and this hiatus may be linked to the decadal shift in the state of the tropical Pacific (Kosaka and Xie 2013, Meehl et al. 2013), the need to thoroughly

assess the time-mean effect of ENSO has become even more apparent.

2. Methodology

2.1 Model Description

The OGCM used in this study is a primitive equation ocean model developed at the state key laboratory of numerical modeling for atmospheric sciences and geophysical fluid dynamics (LASG), Institute of Atmospheric Physics (IAP). It is named as the LASG/IAP Climate Ocean Model (LICOM; Liu et al. 2004a; Liu et al. 2012; Yu et al. 2011). LICOM has been widely applied in studying air-sea interaction, climate change simulation, and it has been shown to be able to simulate realistically the large-sale patterns of oceanic circulation (Liu et al. 2004b; Yu et al. 2007, 2008, 2011).

The version of the model we used is LICOM2.0, which includes some new parameterization schemes, such as a new turbulent mixing scheme (Canuto and Dubovikov 2005), solar radiation penetration, an improved isopycnal mixing scheme (Gent and Williams 1990; Large et al. 1997), etc. In addition, both horizontal and vertical resolutions are enhanced for the upper ocean of LICOM2.0. It is a global ocean model that covers from 75°S to 88°N (the north-pole is treated as an isolated island). In particular, the horizontal resolution is $1° \times 1°$ but the meridional resolution is increased to 0.5° between 10°S and 10°N, and there are 30 layers with 15 equal-depth levels in the upper 150 m. Using climatological monthly-mean wind stress, LICOM2.0 was first integrated from a state without motion to an equilibrium

state through a 500-year spin up. The end state of year 500 is then used as the initial state for the numerical experiments that will be described below.

2.2 Experiment Design

In order to evaluate the model's ability to delineate ENSO variability and further understand the rectification effect of ENSO events onto the climate mean state in the upper Pacific ocean upon the decadal and longer time-scales, one control and two sensitivity runs are designed. The control run has been integrated for 44 years with climatological winds and heat flux, and additionally sea surface temperature and salinity being restored to the Levitus94 datasets (Levitus et al. 1994a, 1994b) as described by Liu et al. (2004b). In those two sensitivity runs, the surface wind stress are climatological winds plus the interannual monthly anomalies, and the surface boundary conditions for temperature and salinity are kept as control run. In the first sensitivity run (hereafter referred to as WSA) that is same as the sensitivity run in SZ2014, the interannual monthly anomalies of 1958-2001 from the European Center for Medium-Range Weather Forecasts 40-years reanalysis (ERA40; Uppala et al. 2005) over the tropical Pacific (120E-80W, 30S-30N) are superimposed on the climatological surface wind stress. The second sensitivity run (hereafter referred to as WSA_R) is as same as WSA except that the sign of the interannual monthly anomalies are reversed.

As we already mentioned in the introduction, the time-mean effect of ENSO

192 delineated in SZ2014 may come from by two factors: the asymmetry of wind stress
193 forcing, or the internal dynamical process in the ocean. The comparison between
194 those two sensitivity runs WSA and WSA_R may help quantify relative the
195 contribution of wind stress forcing and ocean dynamics to the ENSO asymmetry. In
196 this study, the ocean reanalysis from Simple Ocean Data Assimilation (SODA)
197 (Carton and Giese 2004) are compared with model simulations.
198
199 3. Results
200 In this section, we will first show that the observed ENSO variability is well simulated
201 by the model (Section 3.1) (Figs. 1-5). We then contrast the experiments with ENSO
202 (WSA) and that without ENSO to delineate the time-mean effect of ENSO. The
203 differences will be presented as function of seasons (Figs. 6-8). In addition to
204 calculate the NDH for understanding this time-mean effect of ENSO, we also contrast
205 the run in which the ENSO forcing is reversed (WSA_R) with that run without ENSO
206 (control run). One surprising result we will present is that reversing ENSO in the
207 surface forcing does not seem to alter significantly the time-mean effect (Figs. 11-13).
208 We will show that this is because the responses of the current and temperature to the
209 ENSO fluctuations in the surface forcing are largely linear, and thus the perturbation
210 to the velocity the perturbation to the temperature regardless the sign of the ENSO
211 anomaly in the surface winds (Figs. 14-19). The results underscore a fundamental
212 role of the west-east asymmetry in the equilibrium state in the Pacific that is
213 established even in the absence of the ENSO fluctuations (Section 3.2).

3.1 Simulated Mean State and ENSO variability

Climatological mean SST averaged over the whole 44 years from WSA run are shown in Fig. 1b. The figure indicates that the ocean model can reproduce the observed large-scale spatial pattern of SST (Fig. 1a) very well. Some differences between the model simulations and the observations are found in the western warm-pool region—in particular in the region between 120°E and 140°E along the equator where the simulated SST is 0.5 °C higher than the observed. In the cold-tongue region of the central and eastern equatorial Pacific, the simulated SST is 0.5 °C lower than in SODA. The cold-tongue extends a little far to west. In addition, significant warm bias up to 1-2^{o}C in SST is also found in the southeast coast. These biases are very common model biases for almost all the state-of-art OGCMs (Sun et al. 2009). Fig. 1c and Fig. 1d show the temperature in the equatorial upper ocean (averaged between 5°N-5°S) from observations and the model. The figure shows that the basic structure of the observed equatorial thermocline is well simulated by the model although the simulated thermocline around 140°E is a little deeper than the observed.

Fig. 2 shows the seasonal cycle in equatorial SST (showns as deviations from the annual mean temperature). The variation in the simulated SST is dominated by the annual harmonic that peaks at about 100°W, with the warmest SST reached in March and coldest SST reached in September. These features agree well with the observed. The seasonal variations in the eastern equatorial Pacific is in contrast to the seasonal variations in the western Pacific where a semiannual cycle of SST is the most pronounced signal on the equator.

The observed ENSO variability is well simulated by the OGCM as shown in Fig. 3a, which compares the time series of the Nino3 SST from the observed with that from the forced ocean GCM run WSA. The two time series are almost identical. All the observed El Nino and La Nina events are captured by the model simulations. The two time-series have a correlation 0.88 with each other. Note this is higher than the correlation in SZ2014 which is 0.75. The present model has more improvement in simulating the timing—the onset and termination of El Nino events, but the simulated amplitude is still weaker. This discrepancy is expected given that the thermal boundary condition is simplified and the sea surface temperature being restored to the observed climatological datasets (Levitus et al. 1994a, 1994b). The standard deviation of Nino3 index from observation and WSA are respectively 0.91^{o}C and 0.56^{o}C, the simulated variability in magnitude is lower than that in SZ2014 (0.79 ^{o}C). This can be attributed to the experimental design as stated above. Recall that in SZ2014, the restoring SST is zonally uniform and has the value of warm-pool SST. The boundary condition in SZ2014 is based on the theoretical result in Sun (1997) that a zonally uniform SST—warm-pool extending all the way to the eastern Pacific—is an equilibrium solution of the system.

The skewness of the Nino3 index from observation and WSA are 0.68 and 0.44. The probability density functions (PDF) for the Nino3 SST of SODA and WSA are further shown in Figs. 3b-c. The positive skewness in the distribution is evident in both PDFs, although the extreme warm SST anomalies is located at 1.75~2 ^{o}C while the observed

3.25~3.5 °C. This is because the variability is generally weak as evident in Fig. 3a.

The composites of the warm and cold phase SST anomalies are shown in Fig. 4 together with their residuals as another measure of the ENSO asymmetry. Fig. 4 provides the surface condition, in which the selected El Nino events are estimated as the 100 warmest months for the Nino3 region and likewise the chosen La Nina events are from the 100 coldest months for the Nino3 region. In this way, we can gain the same amount of both events, thus the composite analysis can be more reasonable. The method is different from SZ2014, in which a 0.5 °C threshold value for the monthly SST anomaly was used for obtaining the warm/cold events. The major characteristic of the spatial pattern of the SST anomalies are well simulated in the warm/cold phase as well as in the residual. Significant discrepancy with SODA is found in the central Pacific in the cold phase, the negative SST anomalies in the observed spans from 20 °N-20 °S, but in the simulation they are more concentrated in a narrow region of 10 °N-10 °S. Thus the asymmetry feature may be less notable in the central region for the model. Also, the model underestimates the positive SST anomalies in the warm phase which in turn causes an underestimate of the warming in the residual. In general, our model captures the major pattern of the observed asymmetry, implying that the ocean model has enough ability to reproduce ENSO asymmetry and can be used as an effective tool to explore time-mean effect of ENSO and its physical mechanism. Comparing the results with SZ2014, the main discrepancy in the present model is in the warm phase. In the present model, the positive SST anomalies occur in the region

of 15 ℃N-20 ℃N, 180 ℃W-130 ℃W while they agree more with observations in SZ2014. The negative SST anomalies are in better agreement with SZ2014. The differences are expected given the difference in the models. The warming feature in the residual is less pronounced than in SZ2014.

Fig. 5 further shows the corresponding subsurface features from the OGCM and the observed. Just like Fig. 4, the major features of the spatial pattern of the temperature anomalies are well simulated in the warm/cold phase as well as in the residual. The model underestimates the positive temperature anomalies in the eastern Pacific subsurface in the warm phase, which is the main cause of the underestimate of the warming in the residual. In SZ2014, the warming in the eastern Pacific subsurface is also less significant than observations in the residual. Furthermore, the cooling in the residual in the western Pacific subsurface is less significant than the observed in SZ2014, the present model captures the cooling signatures better than SZ2014.

These differences between the two models, while within the typical range of inter-model differences seen in the state of the art ocean models, provides an opportunity to examine whether the rectification found in Sun et al. 2014 is model dependent.

3.2 Time-mean Effect of ENSO

3.2.1 Simulations from WSA

As done in SZ2014, Fig. 6 presents the time-mean (1958~2001) upper ocean temperature (Fig. 6a) and SST differences (Fig. 6b) between the run with ENSO

(WSA) and the run without ENSO (Control). Again, we find that in the presence of ENSO, We have a cooler western Pacific warm-pool and a warmer eastern Pacific cool-tongue. The central equatorial Pacific is also considerably warmer, a feature also shows up in SZ2014. While the major pattern for the rectified effect of ENSO as shown by the present model is the same as SZ2014, there are some differences. For example, the warming center in the equatorial eastern Pacific is located at 100 °W-80 °W, 30~80m, but 100 °W-80 °W, 50~90m in SZ2014; In particular, in 160 °W-120 °W, 0~50m, a warming is shown in SZ2014, but cooling is found in our model. In addition, temperature near the surface between 110 °W-90 °W is decreased in SZ2014 due to the presence of ENSO while in the present model temperature is increased. The extreme warming in SST occurs in the region 100 °W-90 °W, 10 °S-0 in the present model, which agrees that in SZ2014, but another warming SST center in southeast Pacific in SZ2014 is not pronounced in the paper; The warming zone in SST along 5 °N or 5 °S in the central Pacific found in SZ2014 is not found here. Although there exist some differences between the different models, the overall pattern in Fig. 6 resembles closely that in SZ2014.

The seasonal characteristics of ENSO variability in the model SZ2014 used are absent, but our model has. The time-mean temperature differences between simulations with ENSO (WSA) and without ENSO (Control) during four seasons are shown in Fig. 7. The pattern for all seasons resembles Fig. 6a with the warming center occurring between 100 °W-80 °W at 30~80m with the cooling center between 140 °E-180 °E at 100~140m. Despite the spatial pattern in four seasons is similar, the amplitude of

temperature changes varies significantly with seasons. For example, the most obvious warming located at the equatorial eastern Pacific arises in March-April-May (MAM), and the most significant cooling in the equatorial western Pacific occurs in December-January-February (DJF).

Fig. 8 further presents the corresponding surface features for the four seasons. Just like Fig. 7, the overall pattern for all seasons is similar. The major spatial features follow closely Fig. 6b. The warming center is found in the region 110 °W~90 °W and in the eastern boundary 90 °W~80 °W while the cooling center is found near the equator 140 °E~160 °E. There are significant differences across the different seasons. For example, the most significant warming in the eastern Pacific takes place in June-July-August (JJA) while the strongest cooling in the western Pacific is found in September-October-November (SON).

An important suggestion from Liang et al. (2012) is that both ENSO asymmetry and its time-mean effect are caused by the nonlinear dynamical process. As many previous papers (Jin et al. 2003; An and Jin 2004) proposed the nonlinear dynamical heating (NDH) starts from the following SST equation for the heat budget (heat flux and subgrid-scale contributions, e.g., heat diffusion, heat flux due to tropical instability wave are attributed to the term R'):

$$\frac{\partial T'}{\partial t} = -(u'\partial x\overline{T} + v'\partial y\overline{T} + w'\partial z\overline{T} + \overline{u}\partial x T' + \overline{v}\partial y T' + \overline{w}\partial z T') - (u'\partial x T' + v'\partial y T' + w'\partial z T') + R'$$

The NDH can be defined as follows:

$$NDH = -(u'\partial x T' + v'\partial y T' + w'\partial z T')$$

Where T', u', v', and w' are temperature, zonal, meridional and vertical velocities

anomalies, respectively. Fig. 9 gives the time-mean NDH differences between simulations with ENSO (WSA) and without ENSO (Control) during the four seasons. The spatial features in NDH in the equatorial eastern Pacific and temperature differences in Fig. 7 are again found in agreement. For example, the positive NDH in the subsurface generally corresponds to temperature increases. The strongest positive NDH area located at 100 ℃W-80 ℃W, 30~60m in MAM also has a correspondence with the strongest temperature increases in Fig. 7, meanwhile the second strongest temperature changes and NDH occur during DJF. However, the negative NDH in the western Pacific could not illustrate the cooling phenomenon in Fig. 7, because the cooling center in Fig. 7 corresponds to the positive NDH in Fig. 9, it probably implied that NDH does not contribute to the cooling in the equatorial western Pacific.

Fig. 10 then considers the surface features during different seasons. Compare Fig. 10 with Fig. 8, there is a significant correlation between them, especially near the equator. Furthermore, the seasonal variability is identical, the strongest positive NDH in the eastern Pacific including the eastern boundary occurs in JJA, while the most dramatic negative NDH in the western with the positive NDH in the central Pacific arise in SON.

3.2.2 Simulations from WSA_R

To better understand the mechanisms behind the rectified effect of ENSO onto the mean state, in particular, to show that the skewness in the wind stress anomalies applied does not really play a significant role, we have conducted another sensitivity experiment --WSA_R, and compared the rectification in this experiment with that in

WSA. The wind stress anomalies are the same as in WSA but their signs are reversed in WSA_R. This means that the forcing skewness is opposite between these two experiments. Surprisingly, we find that Temperature (Fig. 11a) and SST (Fig. 11b) differences between WSA_R and the control run are highly similar to the corresponding differences between WSA and the control run (compare Fig. 11 with Fig. 6). In other words, even though the external forcing skewness is reversed, the time-mean effect of ENSO remains unchanged, which underscores the singular importance of the nonlinear dynamical process in the upper ocean in rectifying the ENSO into the mean state. There are some noticeable differences, to be sure. For example, temperature cooling in the equatorial western Pacific appears to be more pronounced in WSA_R than in WSA. The temperature warming in the eastern Pacific in WSA extends farther to west than WSA_R (180 ℃W versus 160 ℃W). In addition, it is noted that the warming to the SST in the eastern equatorial Pacific is larger in WSA than WSA_R.

NDH differences between WSA, WSA_R and Control run are shown in Fig. 12. The major pattern in WSA_R resembles that in WSA. There are also noticeable differences. These differences include stronger heating in the central Pacific 180 ℃W ~140 ℃W, 140~200m in WSA_R, and the stronger negative NDH in 130 ℃E ~180 ℃W, 0~60m in WSA_R. Comparing Fig. 12a with NDH in SZ2014 (Fig. 8), the features in the equatorial eastern and western Pacific are identical, but there is the negative characteristic in the central region near the surface 180 ℃W ~100 ℃W, 0~20m while this region has positive NDH in SZ2014. The negative NDH between 160 ℃W

~100 °W at 60~120m in our model also appears to be more profound

Fig. 13 further shows the surface NDH differences. Just that shown in Fig. 12, the overall patterns in WSA and WSA_R are almost identical. The positive NDH in the eastern Pacific along the equator as well as the central Pacific along 5 °N, however, appears to be stronger in WSA_R. In addition, the negative NDH over the warm-pool is more profound in WSA_R too. The main features of the NDH pattern in WSA is consistent with SZ2014, with the exception of the regions 90 °W, 0 ° ~5 °N and 160 °W~120 °W, 0 ° ~5 °S, the present run has the positive NDH while SZ2014 has negative. Although there are differences between our results and those reported in SZ2014, the most momentous regions which show the strongest temperature skewness reach an agreement.

Fig. 14 and Fig. 15 further show the three components of the total NDH presented in Fig. 12 and Fig. 13, respectively. There exists a close resemblance between the zonal component of the NDH and the total NDH, which means that, the total NDH shown in Fig. 12 and Fig. 13 is mostly resulted from its zonal component--the advection of the temperature anomalies by the zonal current anomalies. The magnitude of the meridional and vertical components of the NDH in Fig. 14 are also large, which show the same importance as the zonal component, but in the subsurface they cancel each other. Thus the most important contributor is the zonal component. However, in Fig. 15 the meridional and vertical components of the NDH do not cancel each other in the surface. The meridional component of the NDH in the surface also contributes significantly. All the above results agree with SZ2014. The differences only exist in

detail. The negative meridional component is found at 160 °W~80 °W, 0~20m in Fig. 14 but positive in SZ2014. The negative meridional component in the region 3 °south of the equator in Fig. 15, also the negative vertical component in the equator in Fig. 15, which is different with SZ2014.

Fig. 16 and Fig. 17 help to explain the positive NDH in the equatorial eastern Pacific, Fig. 16 shows the temperature anomalies superimposed by current anomalies averaged in 5 °N~5 °S while Fig. 17 presents the same quantities averaged in 100 °W~80 °W for El Nino and La Nina events. Clearly, the warm phase pattern of WSA is almost identical to the cold phase pattern of WSA_R, while the cold phase pattern of WSA is almost identical to the warm phase of WSA_R, suggesting that the anomalous responses in both the temperature and currents are linear. From Fig. 16, we found that in the warm phase, in the subsurface of equatorial eastern Pacific 100 °W~80 °W，$\partial xT' < 0, \mathrm{u}' > 0$, thus $-u'\partial xT' > 0$, with $\partial zT' < 0, w' < 0$, thus $-w'\partial zT' < 0$，while in the cold phase，$\partial xT' > 0, \mathrm{u}' < 0$, so $-u'\partial xT' > 0$，with $\partial zT' > 0, w' > 0$, so $-w'\partial zT' < 0$. Fig. 17 elaborates the meridional component of the total NDH, $-v'\partial yT' > 0$ in the warm as well as cold phase. In conclusion, the zonal and meridional components of the total NDH play a vital role in inducing temperature increasing in the equatorial eastern Pacific, while the vertical component has the opposite contribution to the strongest positive NDH region; the results appear to be consistent with those in Su et al. (2010).

Why the rectified effect of interannual fluctuations from WSA and WSA_R are mostly same? Fig. 18 and Fig. 19 help to answer this question. The features of annual

mean $\overline{u'T'}$, $\overline{v'T'}$, $\overline{w'T'}$ components are shown in Fig. 18, just as before, WSA and WSA_R have high similarity, except for some small differences in magnitude in some regions, such as 180 °W~160 °W, 120~160m in Fig. 18a, 180 °W~140 °W, 100~200m in Fig. 18c. In order to understand the temperature and current anomalies specifically, we further present Fig. 19 the time-series of u', v', w', T' averaged over the "action centers" shown in Fig. 18 (where the $u'T'$, $v'T'$ and $w'T'$ have their respective maximum values). The temporal variability of u', v', w', T' clearly, the time series in WSA and WSA_R is almost opposite, it means that the u', v', w', T' response to the wind stress anomalies linearly, when make one item multiply another, the results in WSA and WSA_R would be identical. However, the magnitude is not exactly symmetric, in particular, the magnitude in the strongest El Nino years 1997~1998, 1982~1983 is noticeably asymmetric and the magnitude asymmetry leads to the corresponding magnitude discrepancies between WSA and WSA_R in Fig. 18 for these two strongest events.

4. Conclusion

Both the observed and modeling studies reveal a close relationship between the mean state and ENSO variability (Rogers et al. 2004, Liang et al. 2012, Sun et al. 2014, Ogata et al. 2013 among others). In order to unveil the physical mechanism behind this relationship, we have conducted forced ocean experiments to further study the rectification effect of ENSO onto the mean state. The basic methodology follows that of Sun et al. (2014), but a different ocean GCM is employed, allowing to gauge model

456 dependence of the results found in that study. Also, at least in one important aspect,
457 the present GCM is more sophisticated than model used in Sun et al. (2014)—the
458 present model has a seasonal cycle. More importantly, we note that the study of Sun et
459 al. (2014) does not explicitly address the role of the asymmetry of wind anomalies in
460 their forced ocean experiments. Although their basic conclusion about the critical role
461 of nonlinear ocean dynamics will not be affected as the long-term mean wind stress in
462 their two experiments is kept identical. Nonetheless, the curiosity remains about the
463 role of the asymmetry already in the wind stress anomalies applied. So we report here
464 an experiment that Sun et al. (2014) left out. In such an experiment, the wind stress
465 anomalies are reversed in sign. Such an experiment turns out to be helpful in
466 deepening our understanding the role of nonlinear upper ocean dynamics in addition
467 to showing explicitly that the asymmetry or skewness in the wind anomalies plays no
468 role in the rectification as originally anticipated in Sun et al. (2014).
469
470 The major result is that the major features found in Sun et al. (2014) about the
471 rectified effect of ENSO does not dependent on model or has strong seasonal
472 dependence. Our additional experiments—the experiment in which the wind
473 anomalies are revered in sign-- nonetheless shed more light on the mechanisms
474 behind the rectification. The response of the temperature and current in the equatorial
475 upper ocean is both very linear, leading their product to have a single sign. It is
476 speculated that the linear response may have something to do with the strongly
477 asymmetric state in the mean, but further studies are needed to further address this

question

There are also some details in the spatial pattern of the rectification that we want to pursue as future studies. The NDH cannot account for entirely the rectified effect. For example, the cooling in the equatorial far western Pacific probably may not be connected with NDH. Sun et al. (2014) also noted a role of tropical instability waves. The present model has too course spatial resolution to capture this effect, which may explain some differences between the present results and those reported in Sun et al. (2014). It is worth studying the effect of an increase in the resolution of the present ocean model (so that it can better represent the tropical instability waves) on the rectification of ENSO is worth studying.

Acknowledgements. This study is jointly supported by the "Strategic Priority Research Program Climate Change: Carbon Budget and Relevant Issues" of the Chinese Academy of Sciences (Grant No. XDA05110302), and the National Key Program for Developing Basic Sciences Grant No. 2010CB950502. Sun was supported under a grant from US NSF Climate and Large-Scale Dynamics Program (AGS 0852329) and by grants from US NOAA office of global programs--the Earth System Science Program (ESS) and the Modeling, Analysis, and Prediction Program (MAPP).

References

An, S. I., and F. F Jin, 2004: Nonlinearity and Asymmetry of ENSO. *J. Climate*, **17**, 2399-2412.

Battisti, D. S., and A. C. Hirst, 1989: Interannual variability in a tropical atmosphere-ocean model: influence of the basic state, ocean geometry, and nonlinearity. *J. Atmos. Sci.*, **46**, 1687-1712.

Bjerknes, J., 1969: Atmospheric teleconnections from the equatorical Pacific. *Mon. Wea. Rev.*, **97**, 163-172.

Canuto, V. M., and M. S. Dubovikov, 2005: Modeling mesoscale eddies. *Ocean Modeling.*, **8**, 1-30.

Carton, J., and B. Giese, 2004: Simple Ocean Data Assimilation reanalysis effort. In CLIVER Workshop on Ocean Reanalysis.

Delworth, T. L., et al. 2006: GFDL’s CM2 global coupled climate models. Part I: Formulation and simulation characteristics. *J. Climate*, **19**, 643-674.

Gent, P. R., and J. C. McWilliams, 1990: Isopycnal mixing in ocean circulation models. *J. Phys. Oceanogr*., **20**, 150-155.

Jin, F. F., 1997: An Equatorial Ocean Recharge Paradigm for ENSO. Part I: Conceptual Model. *J. Atmos. Sci.*, **54**, 811–829.

Jin, F. F., S. I. An, A. Timmermann, and J. X. Zhao, 2003: Strong El Nino events and nonlinear dynamical heating. *Geophys. Res. Lett.*, **30**, 1120.

Kosaka, Y., and S. P. Xie, 2013: Recent global-warming hiatus tied equatorial Pacific

surface cooling. *Nature*, **501**, 403-407.

Large, W.G., G. Danabasoglu, S. C. Doney, and J. C. McWilliams，1997： Sensitivity to Surface Forcing and Boundary Layer Mixing in a Global Ocean Model: Annual-Mean Climatology. *J. Phys. Oceanogr.*, **27**, 2418–2447.

Levitus, S., T. P. Boyer, 1994a: World Ocean Atlas 1994 Volume 4: Temperature. NOAA Atlas NESDIS 4. US Department of Commerce, Washington D.C., 1-117.

Levitus, S., R. Burgett, T. P. Boyer, 1994b: World Ocean Atlas 1994 Volume 3: Salinity. NOAA Atlas NESDIS 3. US Department of Commerce, Washington D. C., 1-99.

Liang, J., X. Q. Yang, and D. Z. Sun, 2012: The effect of ENSO events on the Tropical Pacific Mean Climate: Insights from an Analytical Model. *J. Climate,* **25**, 7590-7606.

Liu, H. L., P. F., Lin, Y. Q., Yu and X. H., Zhang, 2012: The baseline evaluation of LASG/IAP Climate system Ocean Model (LICOM) version 2. *Acta Meteor. Sinica.*, **26**, 318–329.

Liu, H. L., X. Zhang, Y. Yu, and W. Li, 2004a: Manual for LASG/IAP Climate system ocean model. *Science Press*, Beijing, 1－108pp. (In Chinese)

Liu, H. L., X. Zhang, W. Li, Y. Yu, and R. Yu, 2004b: An eddy-permitting oceanic general circulation model and its preliminary evaluation. *Adv. Atmos. Sci.*, **21**, 675-290.

Meehl, G. A., Hu, J. M. Arblaster, J. Fasullo, and K. Trenberth, 2013: Exernally Forced and Internally Generated Decadal Climate Vairability Associated with the

544 Interdecadal Pacific Oscillation. *J. Climate*, **26**, 7298-7310.
545 Ogata, T., S. P. Xie, A. Wittenberg, and D. Z. Sun, 2013: Interdecadal amplitude
546 modulation of El Nino/Southern Oscillation and its impacts on tropical Pacific
547 decadal variability. *J. Climate*, **26**, 7280-7297.
548 Rodgers, K. B., and P. Friederichs, and M. Latif, 2004: Tropical Pacific Decadal
549 Variability and Its Relation to Decadal Modulations of ENSO. *J. Climate*, **17**,
550 3761-3774.
551 Schopf, P., and R. Burgman, 2006: A simple mechanism for ENSO residuals and
552 asymmetry. *J. Climate*, **13**, 3167-3179.
553 Suarez, M. J., and P. S. Schopf, 1988: A delayed action oscillator for ENSO. *J. Atmos.*
554 *Sci.*, **53**, 2786-2802.
555 Sun, D. Z., 1997: El Nino: A coupled response to radiative heating? *Geophs. Res.*
556 *Lett.*, **24**, 2031-2034, doi:10.1029/97GL01960.
557 Sun D. Z., 2003: A possible effect of an increase in the warm-pool SST on the
558 magnitude of El Nino warming. *J. Climate*, **16**, 185-205.
559 Sun, D. Z., and T. Zhang, 2006: A regulatory effect of enso on the time-mean thermal
560 stratification of the equatorial upper ocean. *Geophs. Res. Lett.*, **33**, L07710,
561 doi:10.1029/2005GL025296.
562 Sun, D. Z., T. Zhang, and S. I. Shin, 2004: The effect of subtropical cooling on the
563 amplitude of ENSO: a numerical study. *J. Climate*, **17**, 3786-3798.
564 Sun, D. Z., T. Zhang, S. Yan, and Y. Yu, 2014: Rectification of El Nino Southern
565 Oscillation into Climate Anomalies Of Longer Time-Scales: Results From Forced

566 Ocean GCM Experiments. *J. Climate*, **27**, 2545-2561.
567 Sun, D. Z., Y. Yu, and T. Zhang, 2009: Tropical Water Vapor and Cloud Feedbacks
568 in Climate Models: A Further Assessment Using Coupled Simulations. *J. Climate*,
569 **22**, 1287-1304.
570 Sun, F. P., and J. Y. Yu, 2009: A 10-15-yr modulation cycle of ENSO intensity. *J.*
571 *Climate*, **22**, 1718-1735.
572 Uppala, S., P. Kallberg, A. Simmons, U. Andrae, V. da Costa Bechtold, M. Fiorino, J.
573 Gibson, J. Haseler, et al., 2005: The era-40 re-analysis. Quart. *J. Roy. Meteor. Soc.*,
574 **131**, 2961-3012.
575 Wittenberg, A. T., 2009: Are historical records sufficient to constrain ENSO
576 simulations? *Geophs. Res. Lett.*, **36**, L12702, doi:10.1029/2009GL038710.
577 Yu, J. Y., and S. T. Kim, 2011: Reversed Spatial Asymmetries between El Nino and
578 La Nina and their Linkage to Decadal ENSO Modulation in CMIP3 Models. *J.*
579 *Climate*, **24**, 5423-5434.
580 Yu, Y. Q. and D. Z. Sun, 2009: Response of ENSO and the Mean State of the
581 Tropical Pacific to Extratropical Cooling/Warming: A Study Using the IAP
582 Coupled Model. *J. Climate*, **22**, 5902-5917.
583 Yu, Y. Q., H. Zhi, B. Wang, H. Wan, H. L. Liu, W. Li, W.P. Zheng, and T. Zhou,
584 2008: Coupled Model Simulations of Climate Changes in the 20th Century and
585 Beyond. *Adv. Atmos. Sci.*, **25**, 641-654.
586 Yu, Y. Q., W. P. Zheng, B. Wang, et al., 2011: Versions g1.0 and g1.1 of the
587 LASG/IAP Flexible Global Ocean-Atmosphere-Land System Model. *Adv. Atmos.*

Sci., **28**, 99–117.

Yu, Y. Q., W. P. Zheng, H. L. Liu, X. H. Zhang, 2007: The LASG Coupled Climate System Model FGCM-1.0. *Chinese J. Geophysics.*, **50**, 1677-1687. (In Chinese)

593 Figure **Legends**

594

595 Fig.1. Climatological sea surface temperature (SST) distribution in the tropical Pacific
596 from SODA (a) and WSA (b). Temperature in the equatorial upper ocean (5^oN-5^oS) as
597 a function of longitude and depth from SODA (c) and WSA (d).

598

599 Fig.2. The seasonal cycle in equatorial SST (5^oN-5^oS) from SODA (a) and WSA (b).
600 Presented are the deviations from their respective annual mean SSTs.

601

602 Fig.3. (a) Nino3 index from the SODA (black line) and WSA (red line). Probability
603 density functions for the SST anomalies of NINO3 region from SODA (b) and
604 WSA(c).

605

606 Fig.4. SST anomalies of ENSO—warm phase (a), cold phase(b) and residual
607 (warm+cold) (c) in WSA (left panels) and SODA (right panels)（Unit:℃）.

608

609 Fig.5. Equatorial upper ocean temperature anomalies of ENSO (5^oN-5^oS)—warm
610 phase(a), cold phase(b) and residual (warm+cold) (c) in WSA (left panels) and SODA
611 (right panels)（Unit:℃）.

612

613 Fig.6. Differences in the time-mean equatorial upper ocean temperature (5^oN-5^oS) (a)
614 and SST (b) between the runs with ENSO (WSA) and without ENSO.

615

616 Fig.7. Difference in the time-mean equatorial upper ocean temperature for the four
617 seasons as a function of depth and longitude between the runs with ENSO (WSA) and

without ENSO.

Fig.8. Time-mean SST difference for the four seasons as function of latitude and longitude between the runs with ENSO (WSA) and without ENSO.

Fig.9. Time-mean NDH difference for the four seasons as function of depth and longitude along equator between the runs with ENSO (WSA) and without ENSO （Unit:℃ $month^{-1}$）.

Fig.10. Time-mean NDH difference as function of latitude and longitude between runs with ENSO (WSA) and without ENSO for the four seasons respectively（Unit:℃ $month^{-1}$）.

Fig.11. Same as Fig.6 but for the run in which the sign of the wind anomalies is reversed—the WSA_R run.

Fig.12. Time-mean NDH difference as function of depth and longitude along equator between the runs with ENSO (WSA) and without ENSO (a) and between the runs with reversed ENSO (WSA_R) and without ENSO (b). Presented are the annual means（Unit:℃ $month^{-1}$）.

Fig.13. Time-mean NDH difference for the surface layer as function of latitude and longitude between the run with ENSO (WSA) and the run without ENSO (a) and between the run with reversed ENSO (WSA_R) and the run without ENSO (b). Presented are the annual mean values（Unit:℃ $month^{-1}$）.

643

644 Fig.14. Same as Fig. 12 but for the three components of the NDH (see text for more

645 details) （Unit:℃ month^{-1}）.

646

647 Fig.15. Same as Fig. 13 but for the three components of the NDH（Unit:℃ month^{-1}）.

648

649 Fig.16. Temperature anomalies (T') along the equator (5^{o}N-5^{o}S) (contours) and the

650 corresponding composite current anomalies (arrows) for the warm phase (a), the cold

651 phase (b) in the WSA run (left panels) and the WSA_R (right panels). Units for the

652 zonal and vertical components of the current anomalies (u' and w') are respectively

653 1m s^{-1} and 1e-5m s^{-1}.

654

655 Fig.17. Temperature anomalies averaged in the eastern Pacific Ocean (100^{o}W-80^{o}W)

656 and the corresponding current anomalies for the warm phase (a) and the cold phase (b)

657 in the WSA run (left panels) and the WSA_R run (right panels). Units for u' and w'

658 are respectively 1m s^{-1} and 1e-5m s^{-1}.

659

660 Fig.18. $u'T'$(a), $v'T'$(b) and $w'T'$(c) runs in the equatorial upper ocean(5^{o}N-5^{o}S), in

661 WSA (left panels) and WSA_R (right panels). We have scaled the w' by H/Lx where

662 Lx and H are respectively half width of the tropical Pacific, and H is the depth of

663 upper ocean (as 400m), and v' by the Ly/Lx where Ly is the Rossby deformation

664 radius on an equatorial beta plane（Unit:℃m s^{-1}）.

665

666 Fig. 19. Time series of u' and T' averaged over the region (170^{o}E, 5^{o}N-5^{o}S) at

667 20m(a); Time series v' and T' averaged over the region(95^{o}W, 5^{o}N-5^{o}S) at 30m(b),

and w' and T' averaged over the region(160°W, 5°N-5°S) at 120m(c) for the WSA run (red line) and the WSA_R run (green line). Yellow shading represents significant El Nino events. We select the regions for which Fig. 18 has the corresponding maximum values for $u'T'$, $v'T'$ and $w'T'$. We have scaled the w' by H/Lx and v' by Ly/Lx.

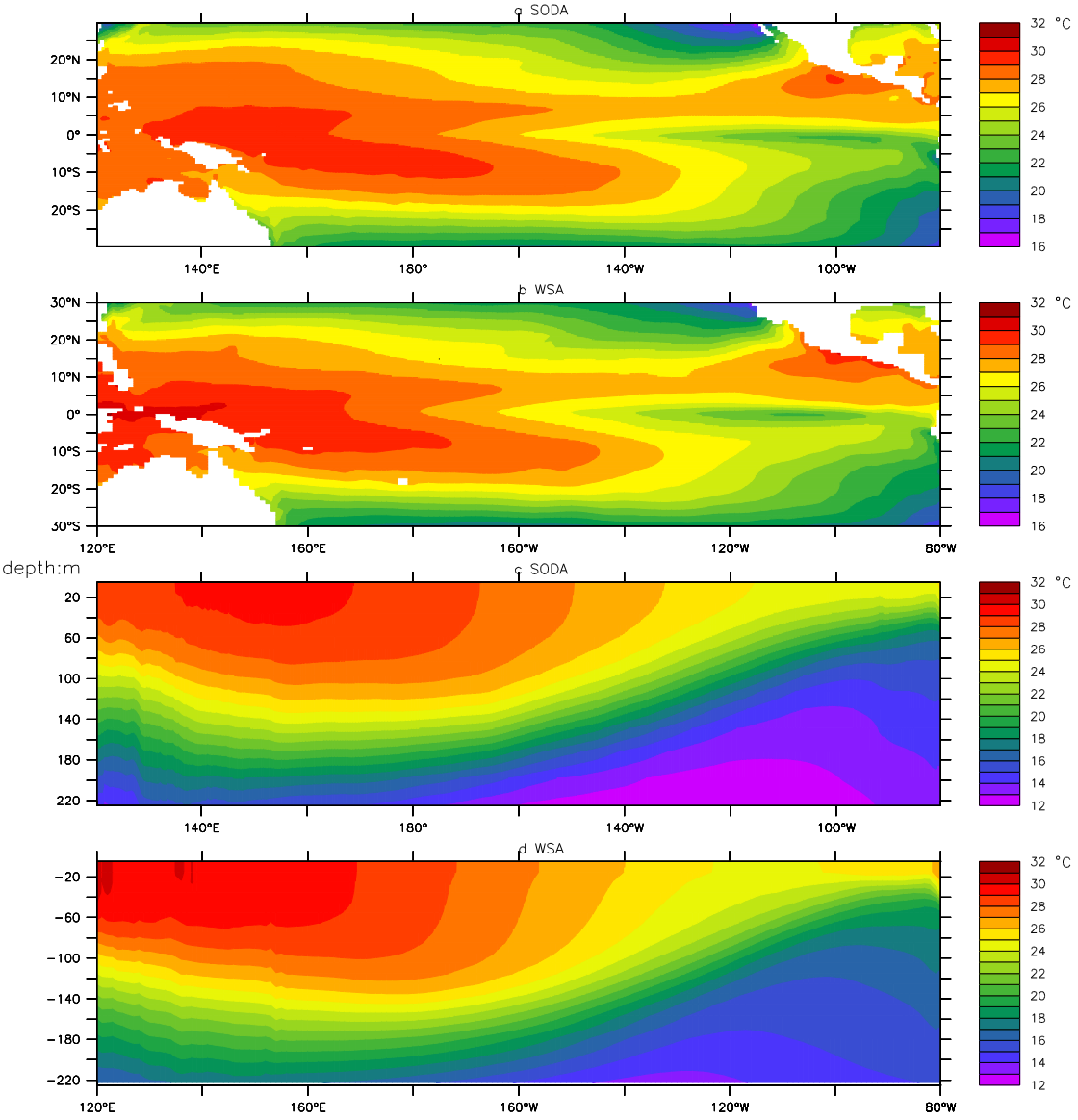

Fig.1. Climatological sea surface temperature (SST) distribution in the tropical Pacific from SODA (a) and WSA (b). Temperature in the equatorial upper ocean (5°N-5°S) as a function of longitude and depth from SODA (c) and WSA (d).

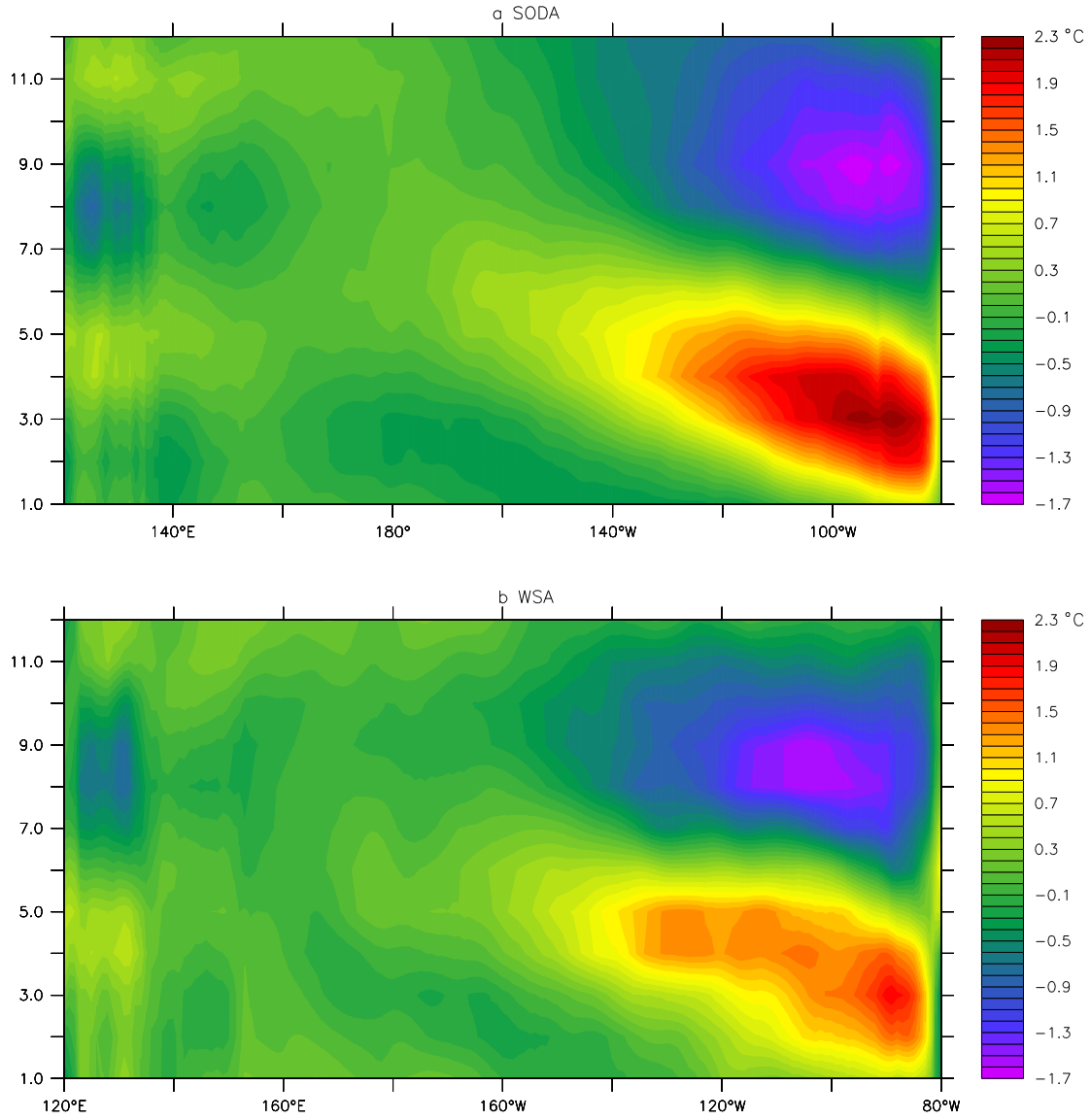

678

679 Fig.2. The seasonal cycle in equatorial SST (5ºN-5ºS) from SODA (a) and WSA (b).

680 Presented are the deviations from their respective annual mean SSTs.

681

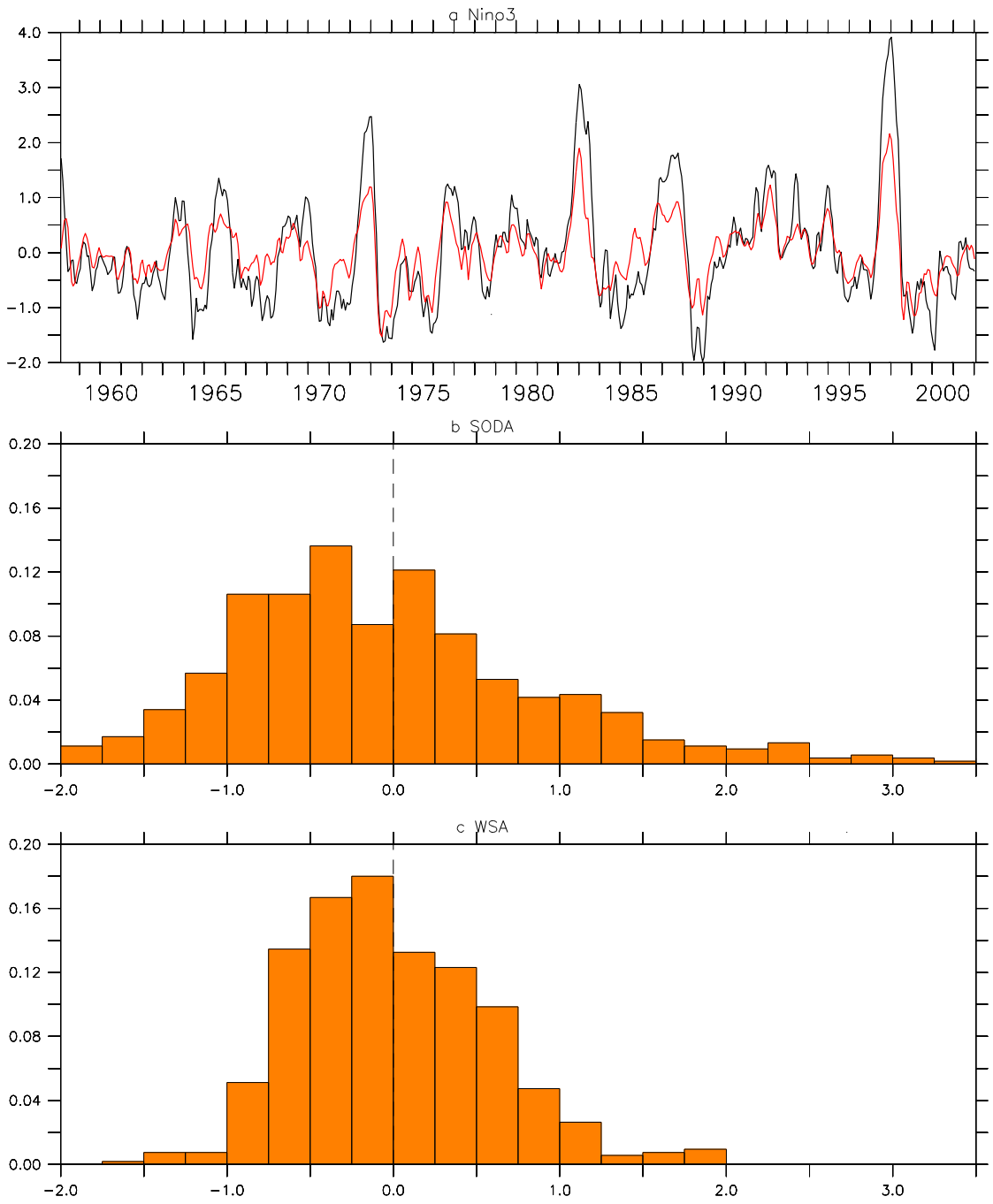

Fig.3. (a) Nino3 index from the SODA (black line) and WSA (red line). Probability density functions for the SST anomalies of NINO3 region from SODA (b) and WSA(c).

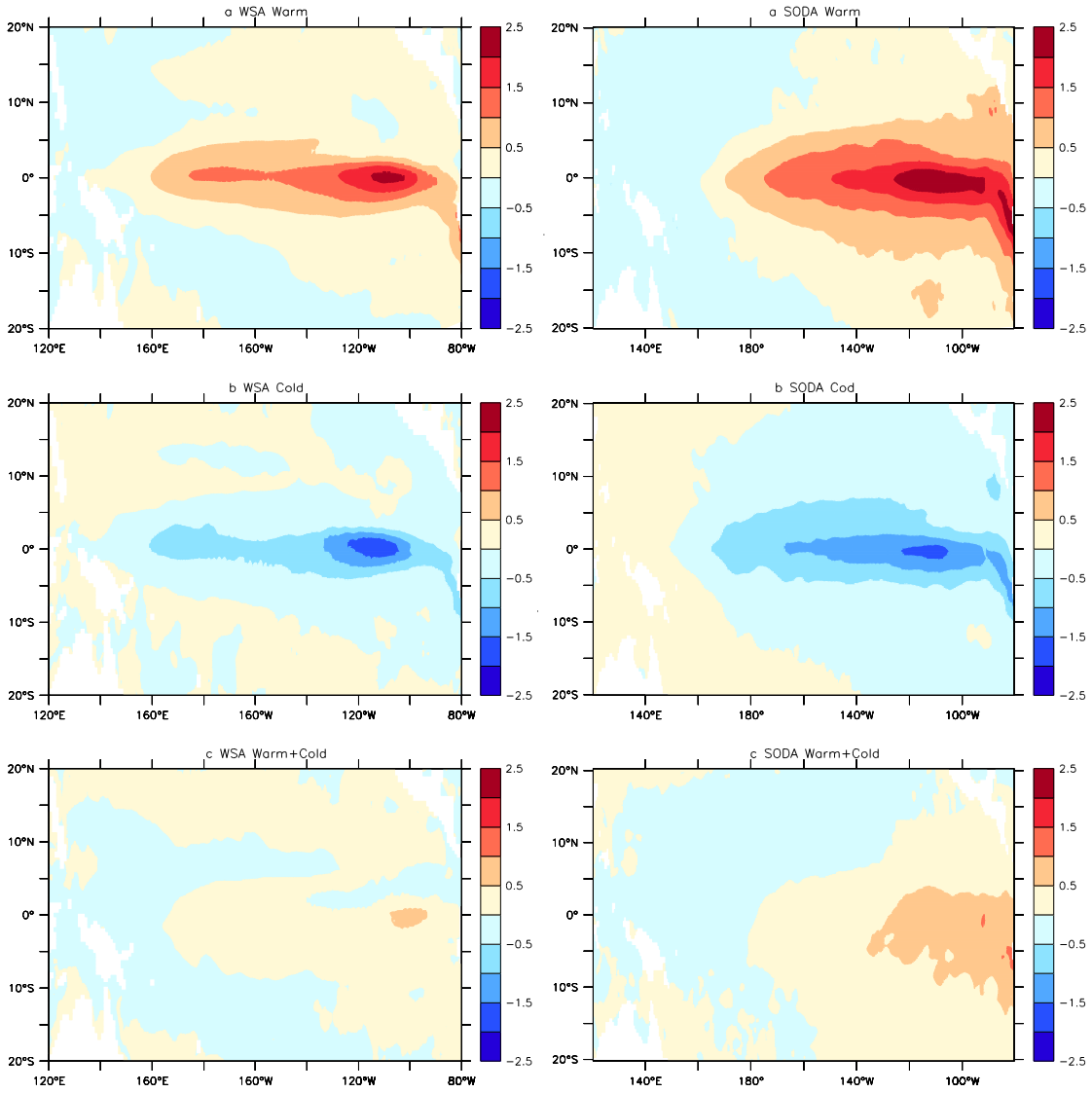

691

692 Fig.4. SST anomalies of ENSO—warm phase (a), cold phase(b) and residual

693 (warm+cold) (c) in WSA (left panels) and SODA (right panels)（Unit:℃）.

694

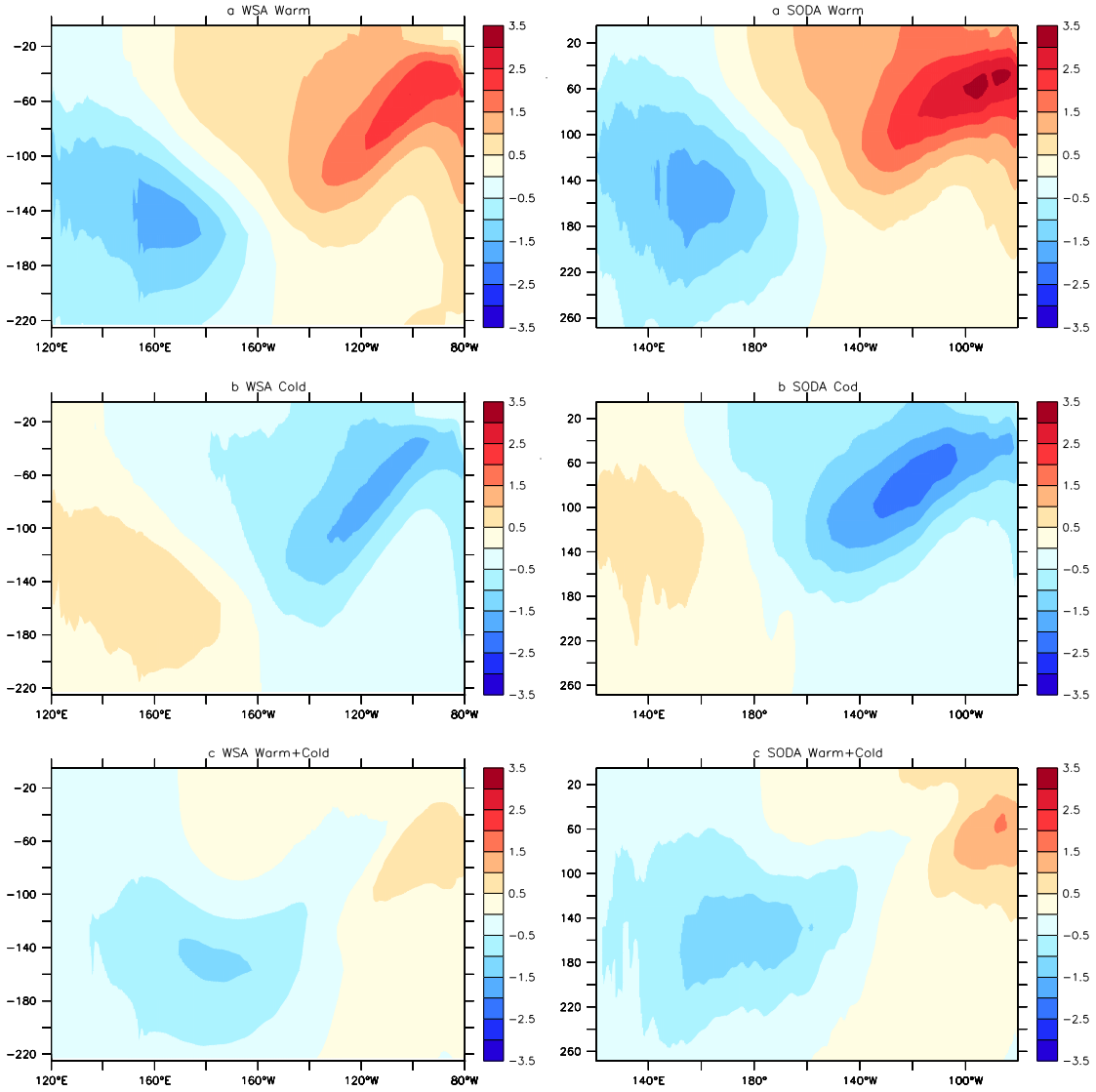

Fig.5. Equatorial upper ocean temperature anomalies of ENSO (5°N-5°S)—warm phase(a), cold phase(b) and residual (warm+cold) (c) in WSA (left panels) and SODA (right panels)（Unit:℃）.

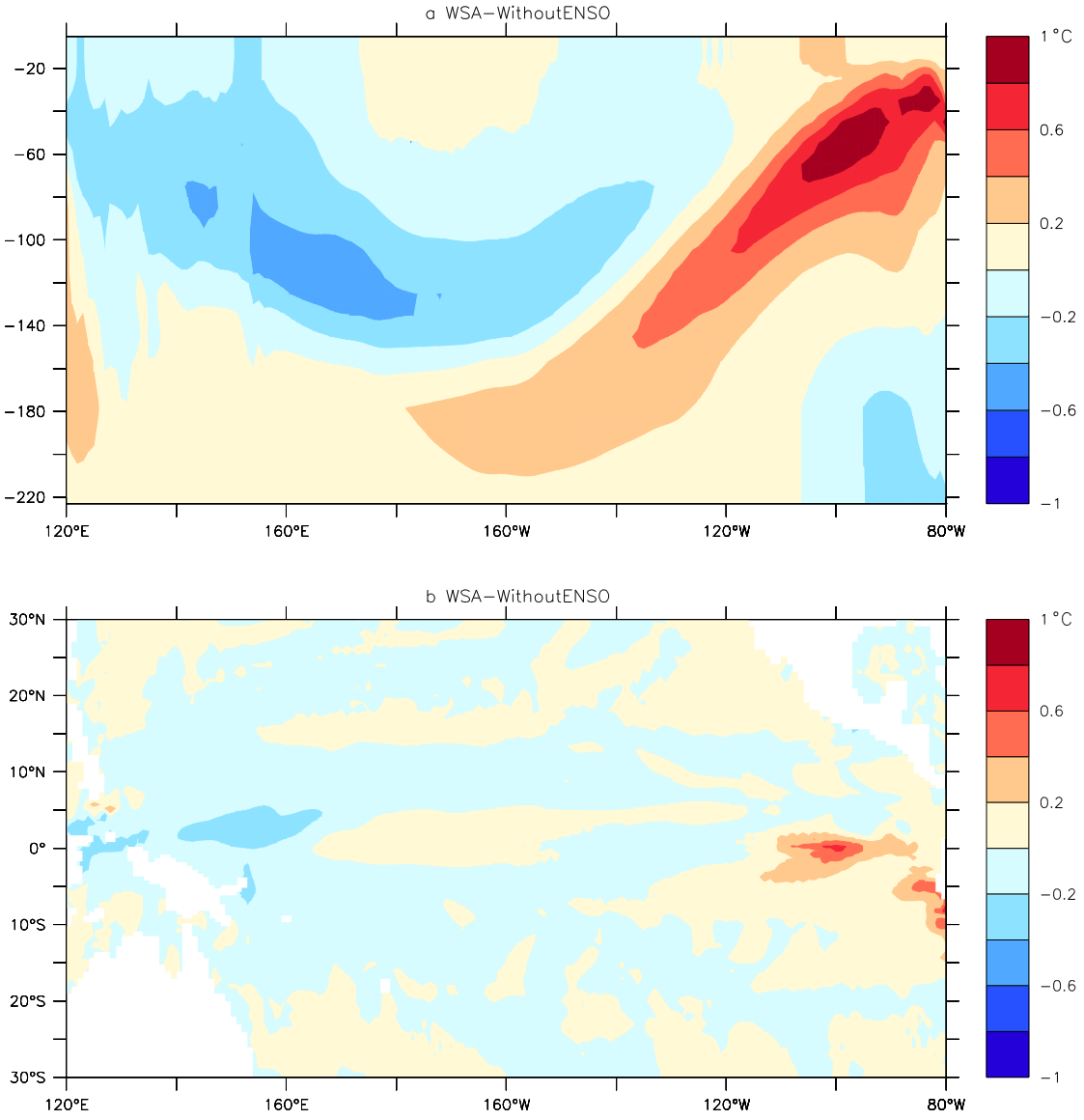

Fig.6. Differences in the time-mean equatorial upper ocean temperature (5^{o}N-5^{o}S) (a) and SST (b) between the runs with ENSO (WSA) and without ENSO.

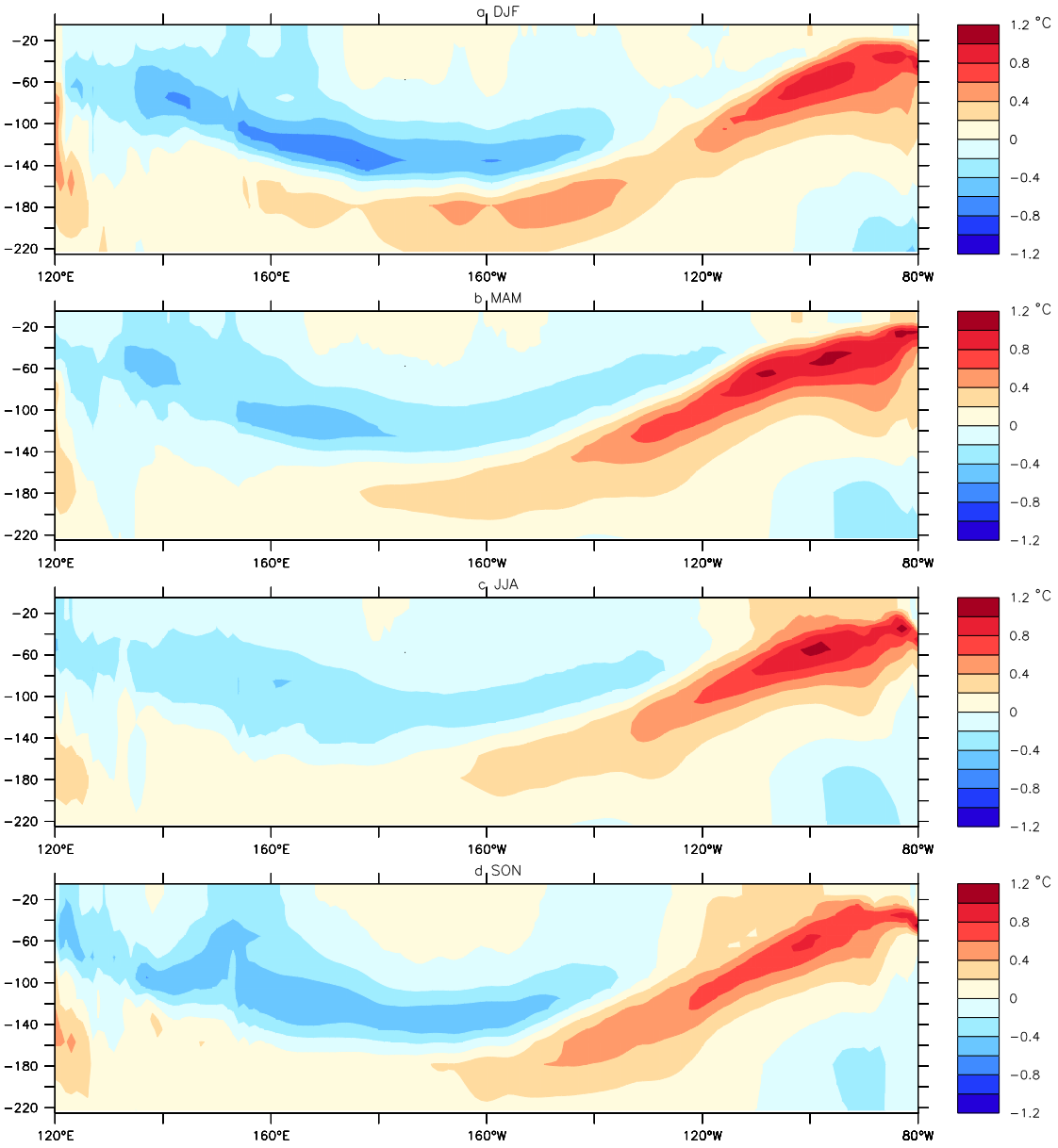

Fig.7. Difference in the time-mean equatorial upper ocean temperature for the four seasons as a function of depth and longitude between the runs with ENSO (WSA) and without ENSO.

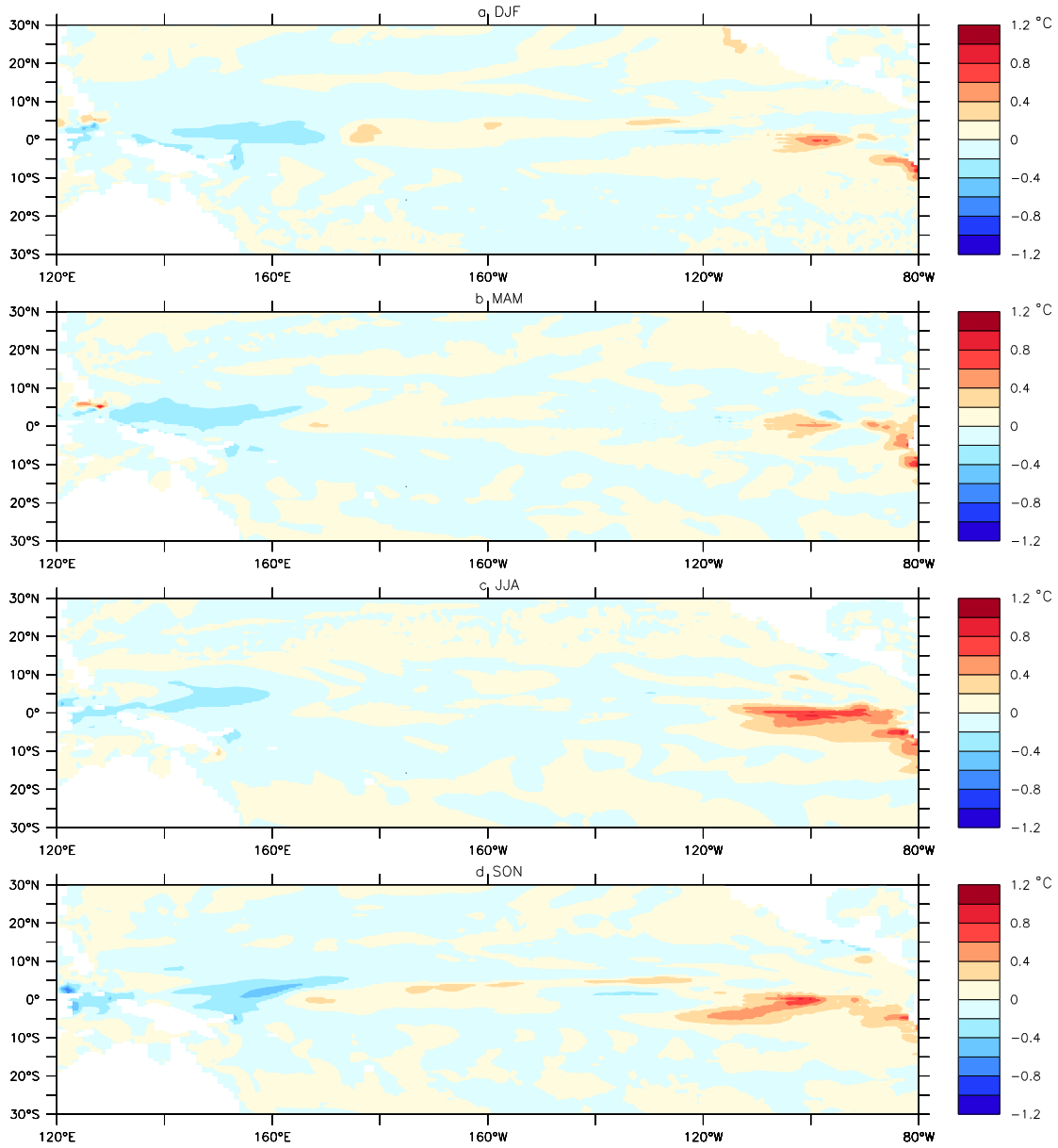

Fig.8. Time-mean SST difference for the four seasons as function of latitude and longitude between the runs with ENSO (WSA) and without ENSO.

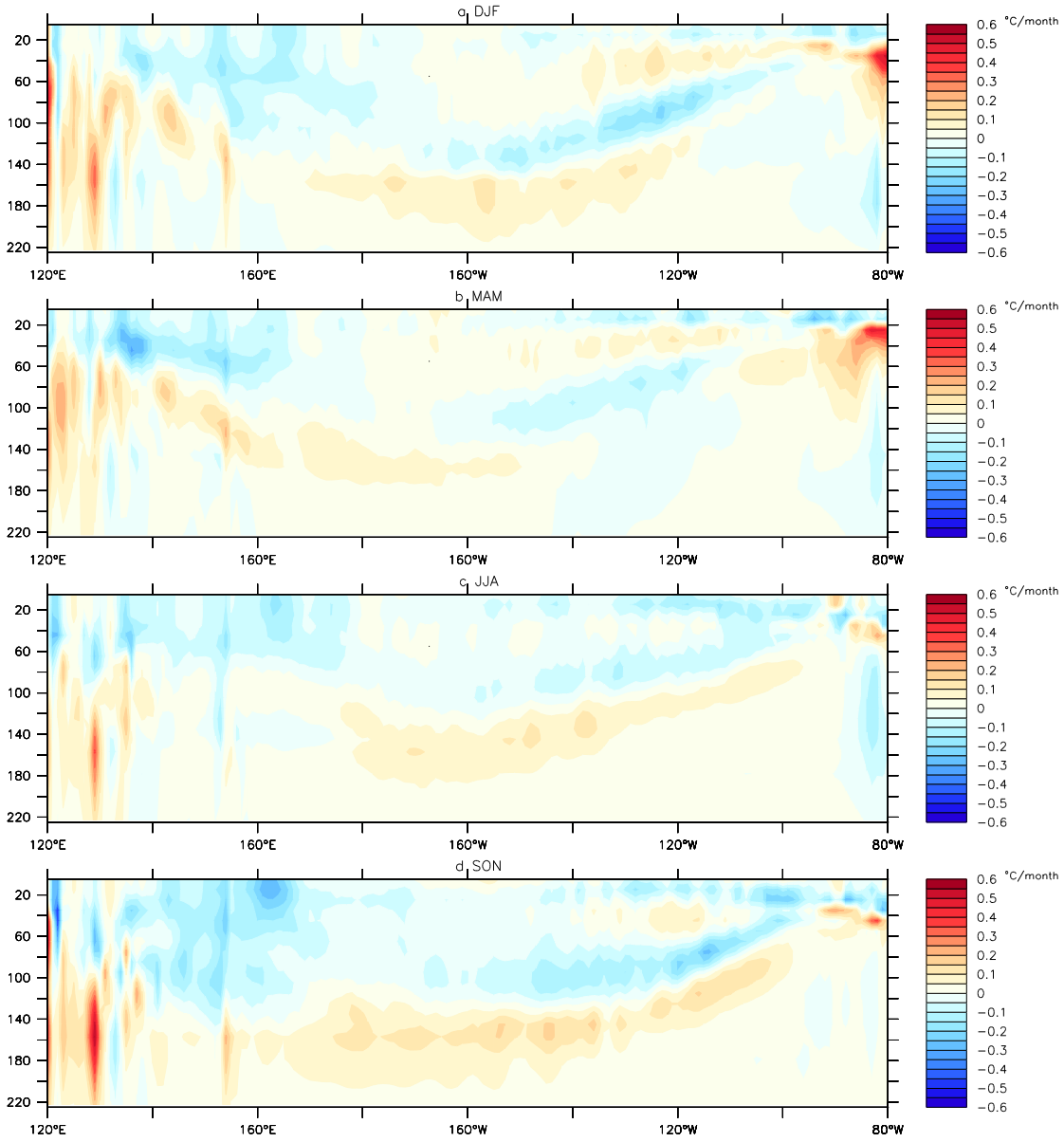

Fig.9. Time-mean NDH difference for the four seasons as function of depth and longitude along equator between the runs with ENSO (WSA) and without ENSO （Unit:℃ month^{-1}）.

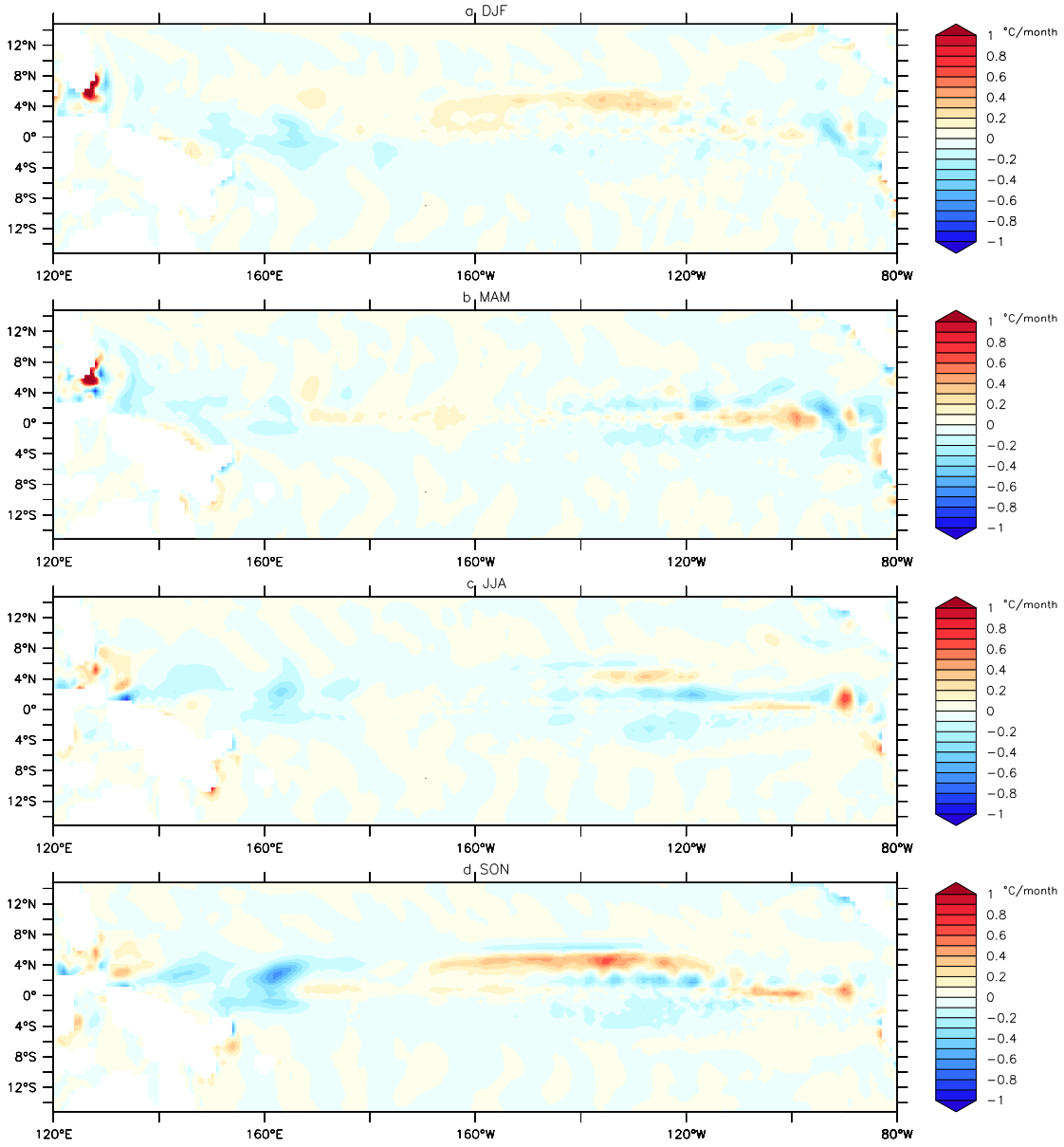

Fig.10. Time-mean NDH difference as function of latitude and longitude between runs with ENSO (WSA) and without ENSO for the four seasons respectively（Unit:℃ month^{-1}）.

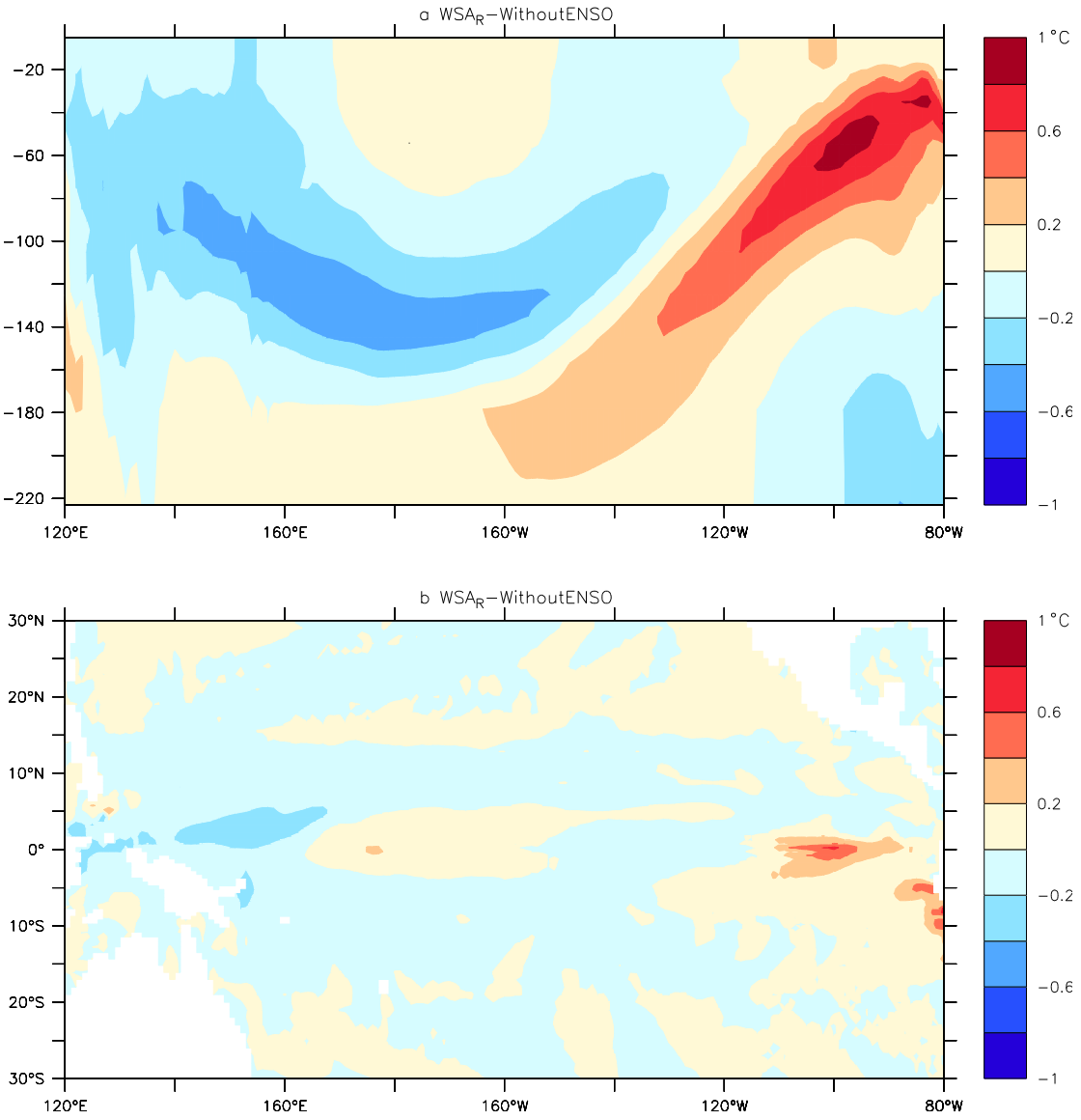

718

719 Fig.11. Same as Fig.6 but for the run in which the sign of the wind anomalies is

720 reversed—the WSA_R run.

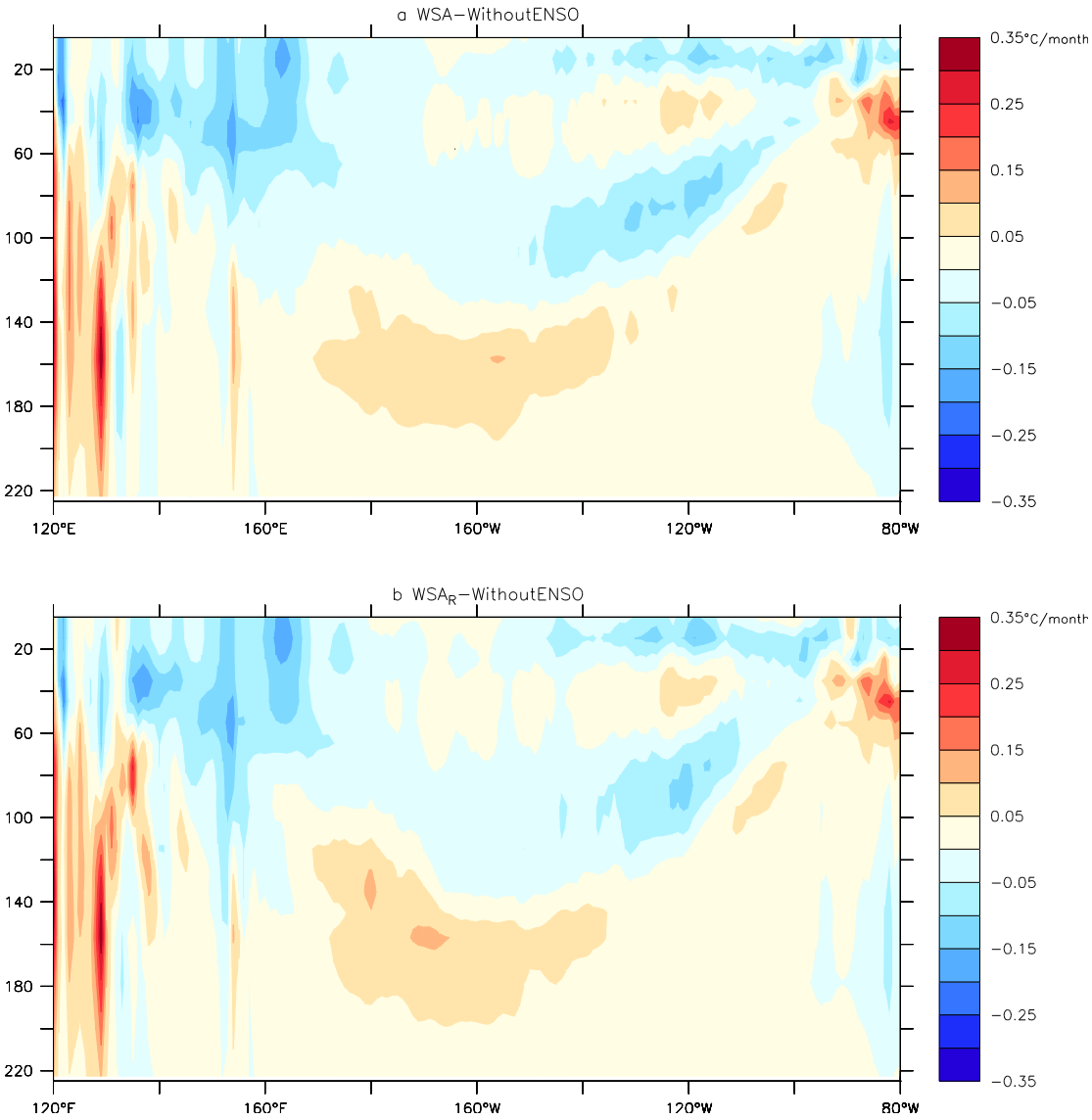

721

722 Fig.12. Time-mean NDH difference as function of depth and longitude

723 along equator between the runs with ENSO (WSA) and without ENSO (a) and

724 between the runs with reversed ENSO (WSA_R) and without ENSO (b). Presented

725 are the annual means（Unit:℃ month^{-1}）.

726

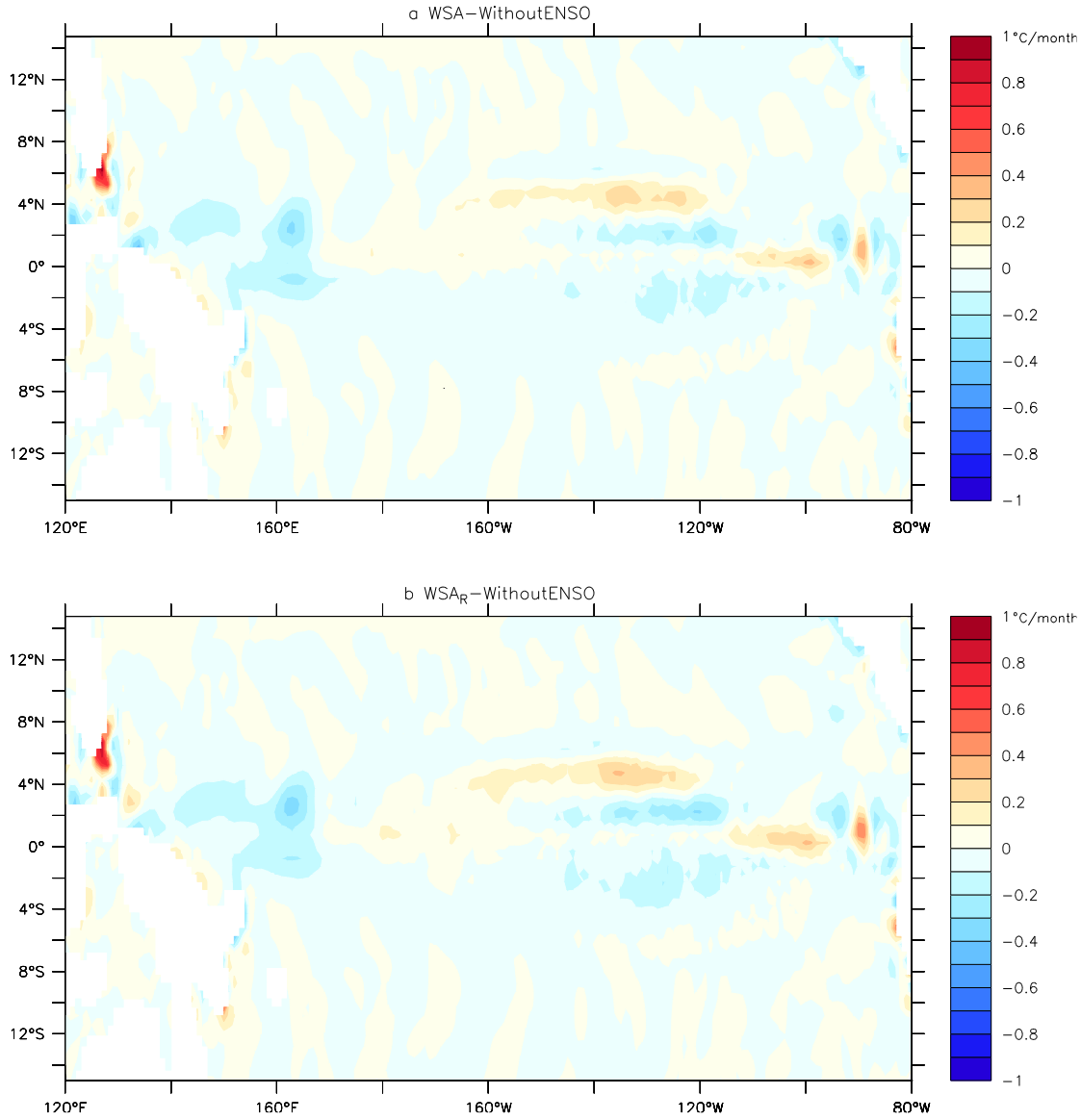

727

728 Fig.13. Time-mean NDH difference for the surface layer as function of latitude and

729 longitude between the run with ENSO (WSA) and the run without ENSO (a) and

730 between the run with reversed ENSO (WSA_R) and the run without ENSO (b).

731 Presented are the annual mean values（Unit:℃ month^{-1}）.

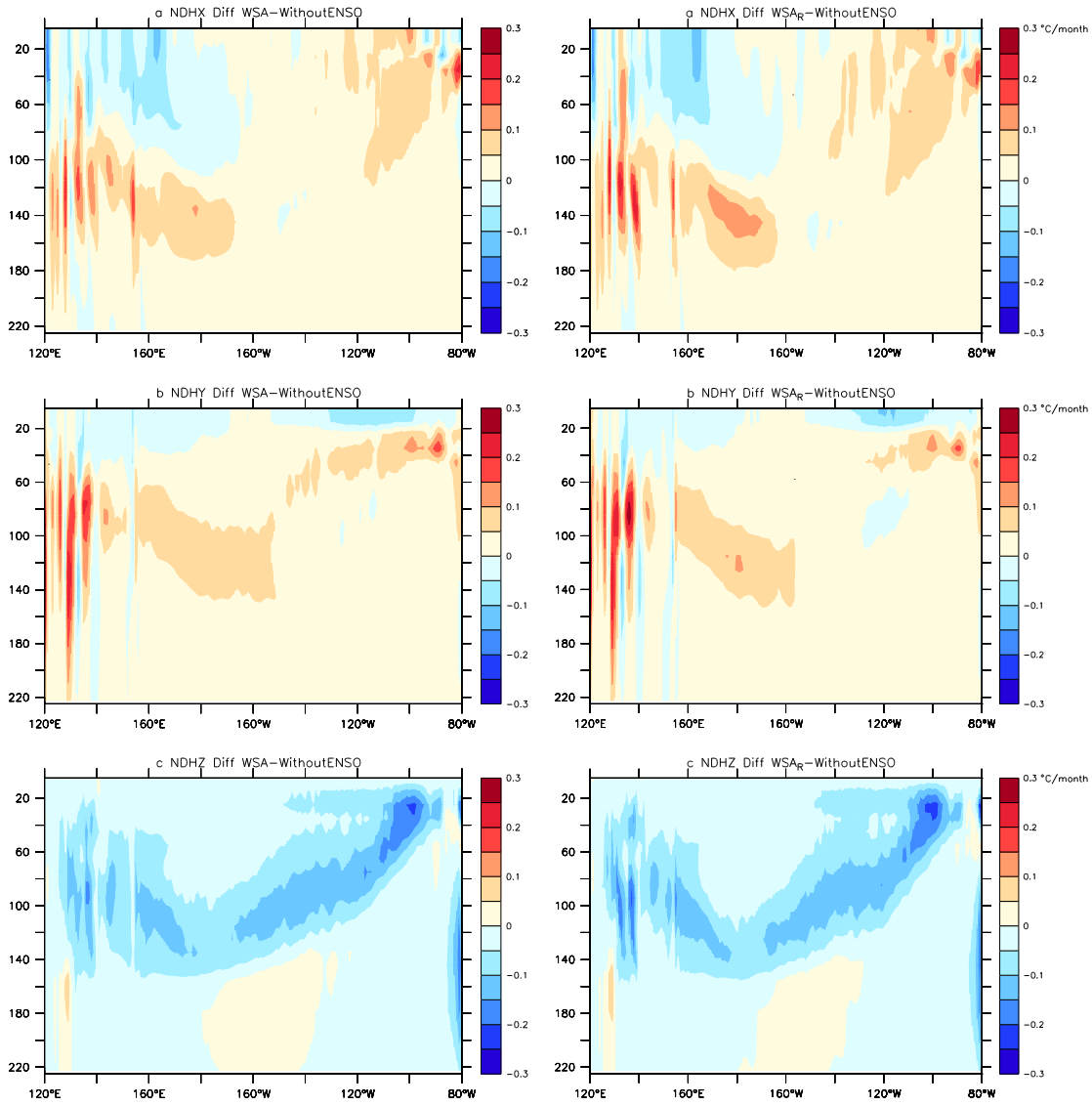

732

733 Fig.14. Same as Fig. 12 but for the three components of the NDH (see text for more

734 details) （Unit:℃ month^{-1}）.

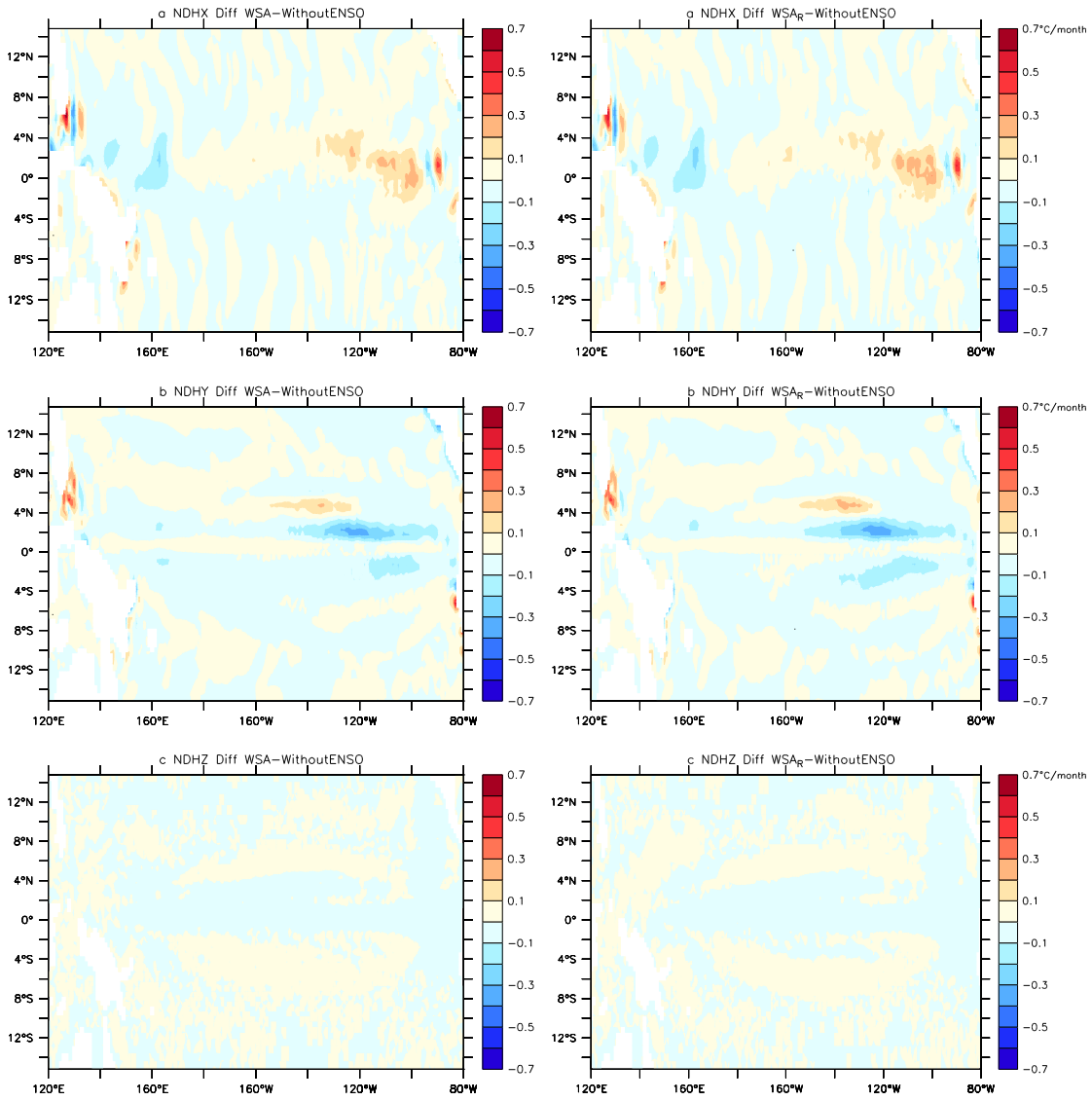

Fig.15. Same as Fig. 13 but for the three components of the NDH（Unit:℃ month^{-1}）.

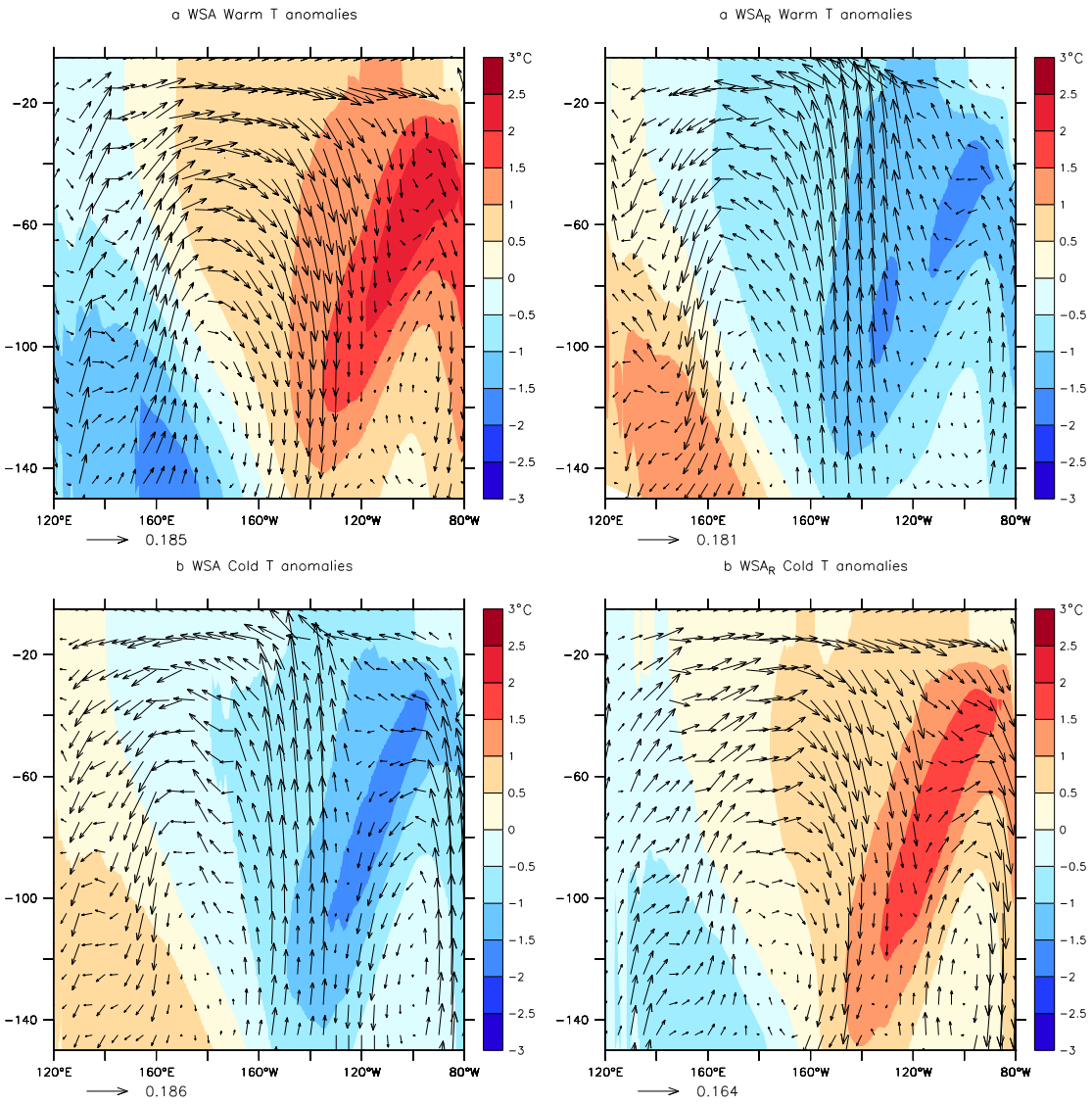

Fig.16. Temperature anomalies (T') along the equator (5°N-5°S) (contours) and the corresponding composite current anomalies (arrows) for the warm phase (a), the cold phase (b) in the WSA run (left panels) and the WSA_R (right panels). Units for the zonal and vertical components of the current anomalies (u' and w') are respectively 1m s^{-1} and 1e-5m s^{-1}.

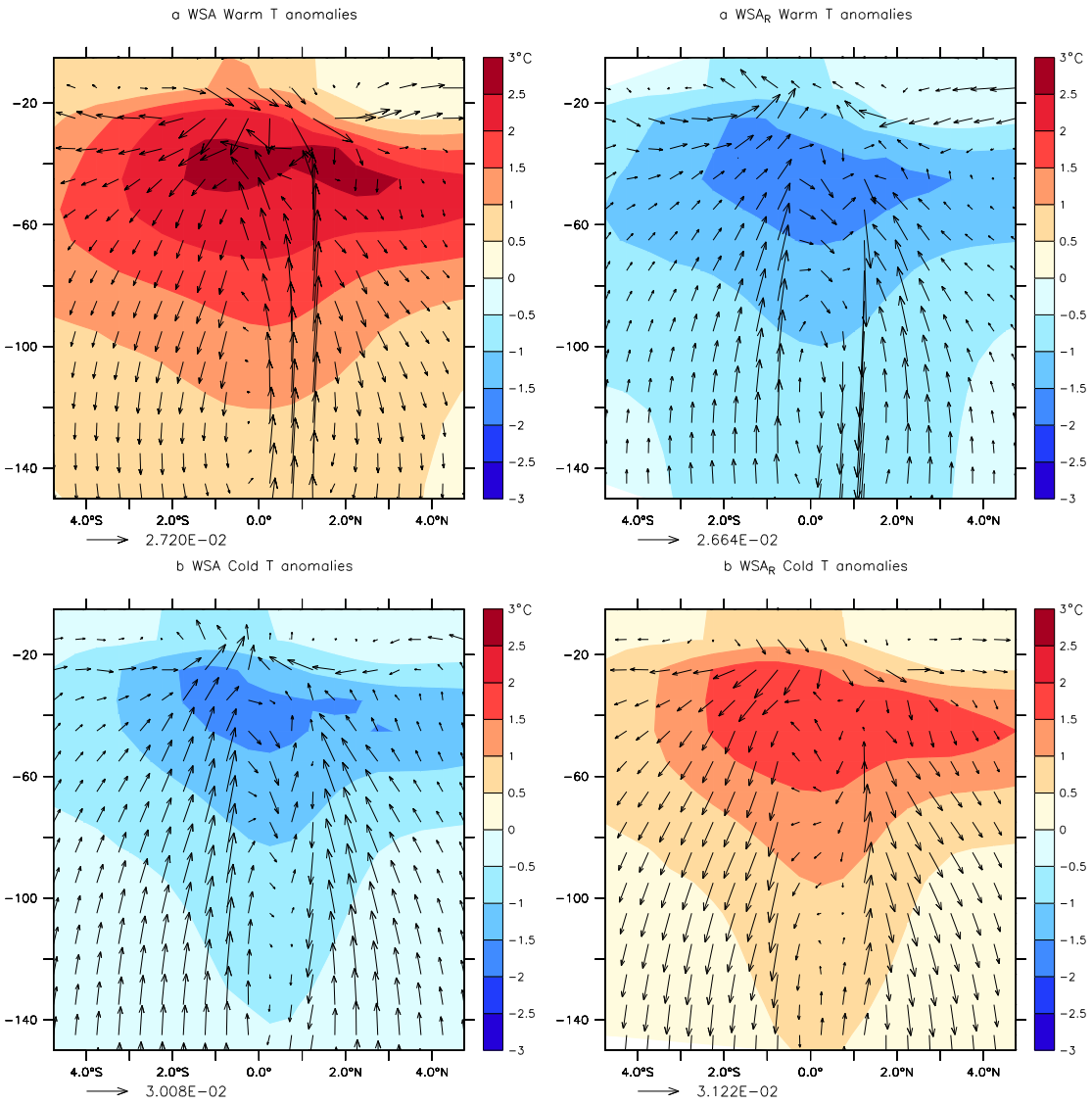

744

745 Fig.17. Temperature anomalies averaged in the eastern Pacific Ocean (100°W-80°W)

746 and the corresponding current anomalies for the warm phase (a) and the cold phase (b)

747 in the WSA run (left panels) and the WSA_R run (right panels). Units for u' and w'

748 are respectively 1m s^{-1} and 1e-5m s^{-1}.

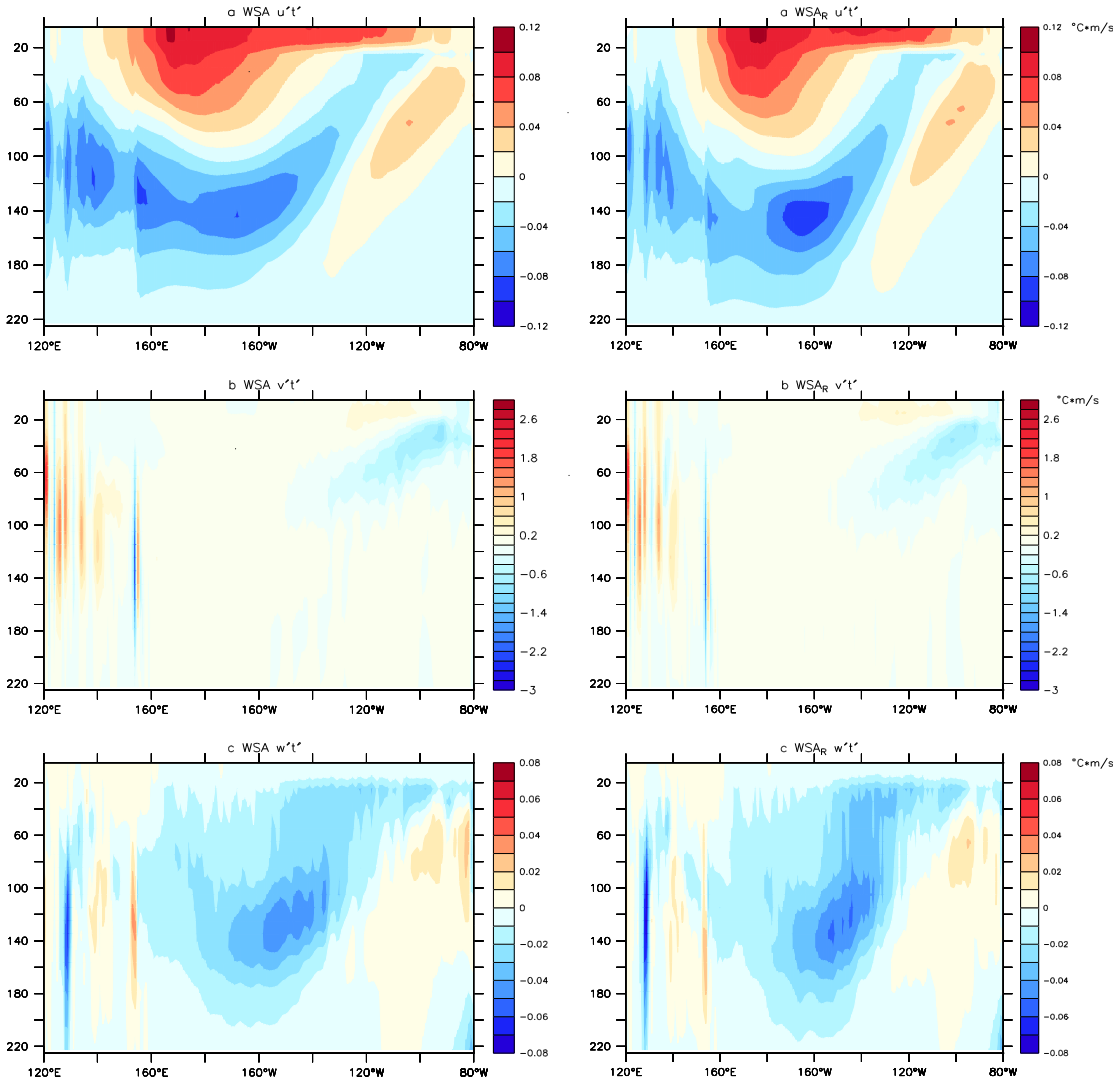

Fig.18. $u'T'$ (a), $v'T'$ (b) and $w'T'$ (c) runs in the equatorial upper ocean(5°N-5°S), in WSA (left panels) and WSA_R (right panels). We have scaled the w' by H/Lx where Lx and H are respectively half width of the tropical Pacific, and H is the depth of upper ocean (as 400m), and v' by the Ly/Lx where Ly is the Rossby deformation radius on an equatorial beta plane（Unit:℃m s^{-1}）.

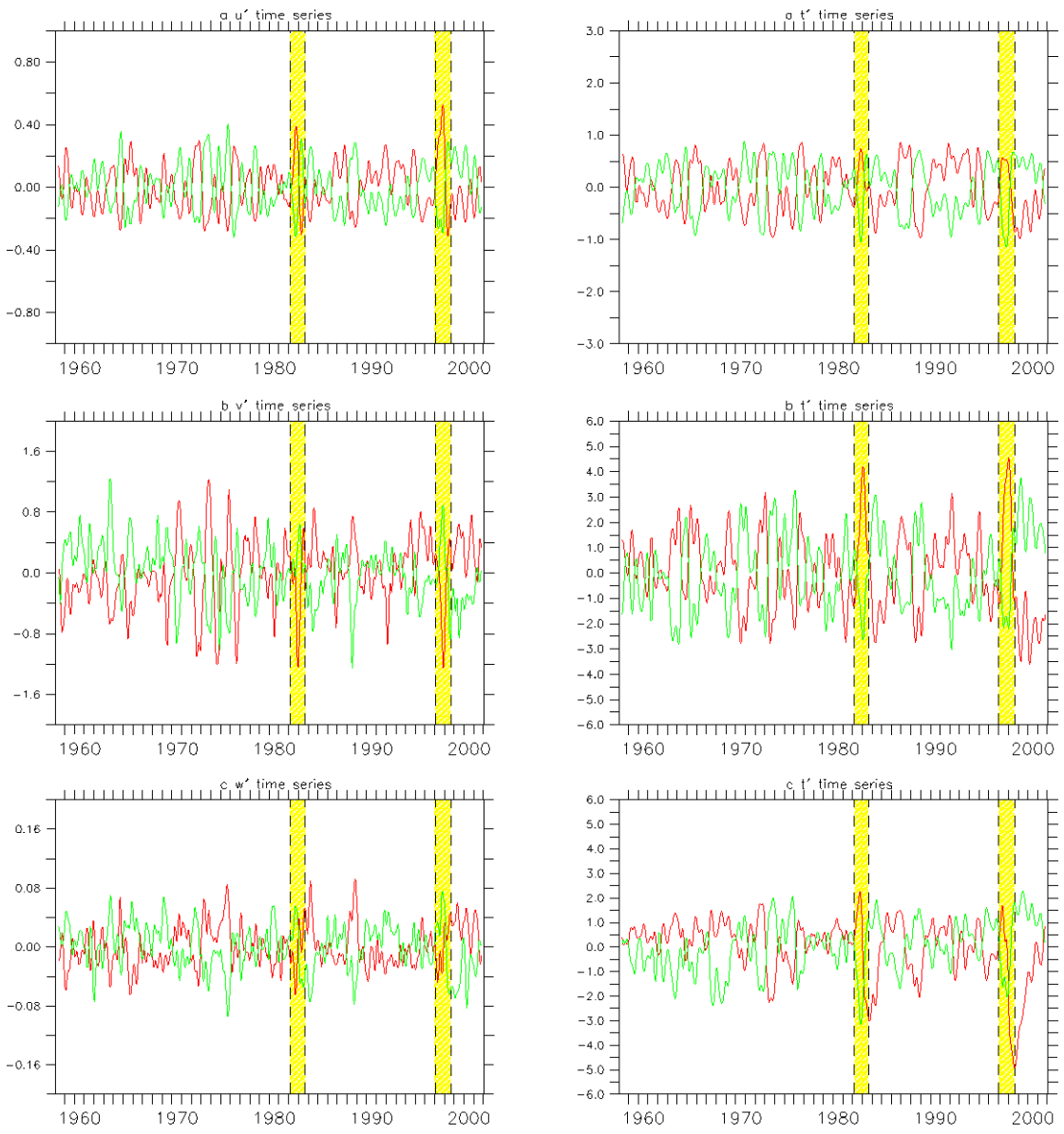

Fig. 19. Time series of u' and T' averaged over the region (170°E, 5°N-5°S) at 20m(a); Time series v' and T' averaged over the region(95°W, 5°N-5°S) at 30m(b), and w' and T' averaged over the region(160°W, 5°N-5°S) at 120m(c) for the WSA run (red line) and the WSA_R run (green line). Yellow shading represents significant El Nino events. We select the regions for which Fig. 18 has the corresponding maximum values for $u'T'$, $v'T'$ and $w'T'$. We have scaled the w' by H/Lx and v' by Ly/Lx.

766
767
768